International Journal of Plasticity 182 (2024) 104114

Contents lists available at ScienceDirect

International Journal of Plasticity

journal homepage: www.elsevier.com/locate/ijplas

A generalised framework for modelling anisotropic creep-ageing deformation and strength evolution of 2xxx aluminium alloys

Xi Wang [a], Zhusheng Shi [a,*], Jianguo Lin [a,b]

[a] Department of Mechanical Engineering, Imperial College London, London SW7 2AZ, UK
[b] Department of Industrial and Systems Engineering, The Hong Kong Polytechnic University, Hung Hom, Kowloon, Hong Kong

ARTICLE INFO

Keywords:
Creep age forming
Anisotropic behaviour
Aluminium alloys
Aluminium-lithium alloys
Modelling framework

ABSTRACT

The 2xxx aluminium alloys are extensively applied in the aerospace industry due to their lightweight and balanced performance characteristics. However, a comprehensive method for modelling both the anisotropic creep deformation and strengthening behaviour in creep age forming (CAF) for 2xxx aluminium alloys remains lacking. This paper presents a generalised framework for establishing constitutive models capable of describing the anisotropic creep deformation coupled with the microstructure and material strength evolutions during creep-ageing of both the original and the pre-deformed 2xxx series Al alloys. This framework extends the rolling direction-based material model to anisotropic scenarios at varying angles between the loading and rolling directions, by employing the non-uniform rational B-splines (NURBS). The details about the anisotropic model calibration and numerical simulation implementation are demonstrated. The feasibility of this method was verified by its application to various 2xxx series aluminium alloys with or without pre-deformation, through constitutive modelling and numerical simulation, with satisfactory agreements between prediction and experimental data. For the first time, the proposed framework provides a generalised routine for establishing anisotropic creep-ageing models for various 2xxx aluminium alloys.

1. Introduction

The 2xxx series aluminium (Al-Cu/Al-Li) alloys have adequately proven their capability as structural components in providing aircrafts with reliable safety and satisfying lifespans throughout their long servicing history (Azarniya et al., 2019; Bodily et al., 2012). A cost reduction in aspects of production and maintenance for aircraft can be made due to their low unit price, acceptable durability and corrosion resistance of the material (Heinz et al., 2000). Furthermore, as a newly introduced alloy grade, the 3rd generation 2xxx Al-Li alloys have been characterised as a more advanced material to replace its predecessors due to its balanced synergy in strength, fracture toughness, and weight reduction (Bodily et al., 2012). On the other hand, the technique for fabricating large panels has made significant advancements since the introduction of creep age forming (CAF) in the 1980s (Zhan et al., 2011a). By inducing creep deformation of the material under elevated temperature, CAF can deform the material below its yield strength. As a result, CAF requires less loading displacement which leads to higher accuracy in the shape control of the deformed material (Wang et al., 2023a; Zhang et al., 2022).

* Corresponding author.
E-mail address: zhusheng.shi@imperial.ac.uk (Z. Shi).

https://doi.org/10.1016/j.ijplas.2024.104114
Received 14 May 2024; Received in revised form 22 August 2024;
Available online 7 September 2024

In the past two decades, the modelling of material creep deformation behaviour in CAF has been transitioned from pure mathematical fitting to mechanism-based prediction, where the latter considers the effect of microstructural evolution of the material on the observed macro creep deformation (Li et al., 2023b). With the adoption of newly introduced advanced aluminium alloys and treatment innovations in recent years, more comprehensive mechanism-based material models have been proposed to cover the observed different creep deformation behaviours in CAF. Li et al. (2016) discovered a double primary creep feature and the presence of a plateau in the primary creep-ageing stage of the 3rd generation Al-Li alloy AA2050-T34 and successfully explained this material behaviour with the concurrent precipitation of new precipitates and dissolution of existing clusters, based on which a mechanism-based material model able to capture these deformation characteristics was established (Li et al., 2017). Zheng et al. (2018) proposed a material model for multi-step creep-ageing of a 7xxx series aluminium alloy at 120 °C for 6 h followed at 177 °C for 7 h. This model yields satisfying prediction agreements with experimental data of the macro creep deformation and microstructural evolutions at each ageing step. By considering the effect of threshold stress evolution, Yang et al. (2020) and Rong et al. (2021) respectively modelled the identified nonlinear variation of creep deformation with stress levels. Those methods shed light on predicting the creep behaviour of aluminium alloys in CAF when anisotropic creep deformation is not a concern.

In recent years, as an increasing demand has emerged for CAF fabrication of panels with more complex contours, the anisotropic issue of the material and its effects on creep-ageing have been more extensively investigated. Strong in-plane anisotropy (IPA) for material strength and creep deformation was respectively identified for AA2524-T3 and AA2219-T3 by Xu et al. (2018) and Chen et al. (2020). Both studies attributed the observed anisotropic behaviours to the varying values of Schmid factor and equivalent sliding system for the material textures at different loading orientations. Bian et al. (2020) also pointed out that for the observed anisotropic behaviour of AA7050 in creep-ageing, the equivalent Schmid factor and slip system number determined by the material texture at different directions can exert significant effects. Besides the material texture, recent investigations also identified the influences of different pre-treatments on material anisotropy. Chen et al. (2021b) and Xia et al. (2023) respectively investigated the effects of different pre-treatments on the anisotropy of AA2196 and AA2195. In both studies, the observed anisotropy reduction was attributed to the incubation of more uniformly distributed T_1 precipitates with different treatments. Peng et al. (2022) and Chen et al. (2022) identified the effects of dislocation and the dislocation formed cell structure on the material anisotropy. The former found that the interactions of mobile dislocations with geometrically necessary dislocations (GND) can exert substantial effects on material anisotropy, and the latter focused on the influence of the morphology of the dislocation cells formed with large pre-deformation.

Though extensive efforts and solid progresses have been made for investigating the material anisotropy in creep-ageing, establishing the material model to capture the anisotropic creep-ageing behaviour remains a critical challenge. Tong et al. (2020) attempted to express the creep anisotropy through a phenomenological method by introducing parameters into the creep-ageing material model to directly fit the obtained experimental creep strain results at each direction. Peng et al. (2022) further proposed a mechanism-based model which can achieve satisfactory agreements with the experiment results at both micro and macro scales including creep deformation and precipitate evolution. However, three sets of material constants were separately determined using the experimental data at 0°, 45°, and 90°, leading to the question of the prediction accuracy at other directions and the adaptability in numerical simulation. More recently, Chen et al. (2022) established a material model able to continuously predict the anisotropic creep deformation behaviour from 0° to 90°, by considering the different long range internal stress induced by the dislocation cell (DC) morphology in the largely deformed AA2195. However, question remains regarding the application of the model in numerical simulation. By introducing an anisotropic parameter and treated it as a non-uniform rational B-spline (NURBS) function of angle θ to the rolling direction, Wang et al. (2023b) succeeded in capturing the observed anisotropic creep behaviour of a 3rd generation Al-Li alloy in creep-ageing through modelling and numerical simulation. On the other hand, by considering the resistance differences caused by four variants of T_1 precipitates, a modelling framework is proposed to predict the anisotropic yield strength for Al-Li alloys with different processing conditions (Zhao et al., 2022). Despite the progresses in anisotropic modelling for continuous prediction of material creep-ageing behaviour at changing loading angles, there is still the need for a generalisable framework to construct anisotropic creep deformation models for aluminium alloys with different temper and varying treatment conditions.

Considering the significance of applying 2xxx aluminium alloys to fabricate large panel components with more complex contours, as well as the need to capture material anisotropic creep deformation behaviour in CAF fabrication process, it is of substantial urgency to establish a feasible method for constitutive modelling to address the anisotropic issue. In addition, with the growing focus on employing pre-deformation treatment to overcome the low formability issue of high strength aluminium alloys in CAF (Chen et al., 2021a; Liu et al., 2020), it is essential to adequately capture pre-deformation treatment effect on the anisotropic behaviour in the subsequent creep-ageing through material modelling. Therefore, this study aims to provide a generalised framework for establishing constitutive models capable to describe the anisotropic creep deformation coupled with the evolutions of microstructure and material strength during creep-ageing for the 2xxx series Al alloys in various states. The proposed method is characterised by the following advances: (1) By employing NURBS-expressed anisotropic coefficients in the rolling direction-based material model, a comprehensive prediction including material deformation and hardening behaviour coupled with microstructural evolution at varying loading angles of various 2xxx series aluminium alloys can be achieved. (2) The establishment of the constitutive relation between macro pre-deformation and changes in micro dislocation structure morphology allows for modelling the effects of pre-deformation-induced internal stress variation on material anisotropy in creep-ageing. (3) The proposed framework is able to establish models for various 2xxx Al alloys which can adequately capture the anisotropic creep deformation and strengthening behaviours in creep-ageing and can be successfully implemented in numerical simulation. This framework guarantees the consistency between the model predicted equivalent strain and the measured strain at varying loading angles, which is of significance in ensuring the feasibility and prediction accuracy when utilising the model in numerical simulation of CAF process.

2. Framework for modelling anisotropic creep-ageing

This section presents a generalised framework for establishing anisotropic creep-ageing material model. In the first step of the framework, a constitutive model is established with three sub-models, respectively for microstructural evolution, loading direction-based stress-creep strain relation, and material strengthening. The established model can be adopted to describe the anisotropic micro scale dislocation and precipitate evolutions, as well as macro creep deformation of the 2xxx series aluminium alloys at various temper conditions and with different pre-deformation treatments. In the second step of the framework, a general routine for model calibration and application in CAF numerical simulation is provided for anisotropic scenarios.

2.1. The rolling direction-based material model

A previously proposed rolling direction-based non-anisotropic material model (Wang et al., 2022b), which is capable of expressing creep deformation when loaded in both the elastic range and the plastic range, is adopted as a fundamental model in this study. This model can be summarised as being composed of three sub-models with each presented from Eq. (1) to Eq. (3) detailed below.

The evolutions of precipitates and dislocations are the main microstructures which can exert the most significant effects on creep deformation behaviour of the material during creep-ageing. Grain size is important in dynamic recrystallisation but rarely changes during creep-ageing. Therefore, for the convenience and adaptability of the model in practical use, most of the mechanism-based creep-ageing material models quantitatively take the normalised dislocation density ($\overline{\rho}$) and precipitate radius ($\overline{r}$) as the two key microstructural evolution variables (Wang et al., 2022b; Zhan et al., 2011b). The microstructural evolution sub-model is shown below:

$$\varepsilon_p = (\sigma - \sigma_{end})/E + K(\sigma - \sigma_{end})^{n'} \tag{1–1}$$

$$\dot{\overline{\rho}}_0 = A_1(1-\overline{\rho}_0)\left|\dot{\overline{\varepsilon}}_p\right|^{m_1} - C_p\overline{\rho}_0{}^{m_2}\left|\dot{\overline{\varepsilon}}_p\right|^{m_5} \tag{1–2}$$

$$\dot{\overline{\rho}} = A_1(1-\overline{\rho})\left|\dot{\overline{\varepsilon}}^{cr}\right|^{m_1} - C_p\overline{\rho}^{m_2}\left|\dot{\overline{\varepsilon}}^{cr}\right|^{m_5} \tag{1–3}$$

$$\begin{cases} \dot{\overline{r}} = C_r(Q-\overline{r})^{m_3}(1+\gamma_0\overline{\rho}^{m_4})Q = Q_1/(1+\varepsilon_{PD})^{m_6} \end{cases} \tag{1–4}$$

where the dot above a variable stands for the time derivative, i.e. the evolution rate, E is Young's modulus, K, n', A_1, m_1, C_p, m_2, m_5, C_r, Q, m_3, γ_0, m_4, Q_1, m_6 are materials constants.

In Eq. (1–1), $\overline{\varepsilon}_p$ represents the accumulated equivalent plastic strain during the loading stage of creep-ageing when the applied stress σ surpasses the linear elastic stress-strain limit σ_{end}. In Eq. (1–2), $\overline{\rho}_0$ stands for the normalised dislocation density accumulated in the loading stage when surpassing the elastic region. $\overline{\rho}_0$ is defined as $(\rho_0 - \rho_i)/\rho_m$, where ρ_i represents the dislocation density at the as-received state, ρ_m is the dislocation density at the saturated state. Based on the definition, value of $\overline{\rho}_0$ ranges from 0 to 1. When the applied stress is within the linear stress-strain relation i.e. $\sigma < \sigma_{end}$, the values of ε_p and $\overline{\rho}_0$ are 0. In Eq. (1–3), $\overline{\varepsilon}^{cr}$ is the equivalent creep strain; $\overline{\rho}$ is the normalised dislocation density accumulated in the creep-ageing stage as $\overline{\rho} = (\rho - \rho_i)/\rho_m$ with its value at the beginning of creep-ageing equalling to the final value of $\overline{\rho}_0$. In the case of large pre-deformation where dislocation recovery dominants and leads to a reduction in dislocation density (Chen et al., 2022; Liu et al., 2020), $\overline{\rho}$ is employed as $\overline{\rho} = \rho_i/\rho_m$ with an initial value of 1 for creep-ageing. In addition, the factors $\left|\dot{\overline{\varepsilon}}_p\right|^{m_5}$ and $\left|\dot{\overline{\varepsilon}}^{cr}\right|^{m_5}$ are respectively introduced into Eq. (1–2) and (1–3) to include the effect of strain rate on dislocation annihilation by dynamic recovery (Chen et al., 2022). Eq. (1–4) shows the evolution of precipitate size. $\overline{r}$ is the normalised precipitate radius expressed as $\overline{r} = r/r_c$, where r and r_c are respectively the average precipitate size during creep-ageing and at its peak-age state. The effect of pre-deformation on precipitation growth is considered with the introduction of the term $(1+\varepsilon_{PD})^{m_6}$ in Eq. (1–4), where ε_{PD} represents the pre-deformation extent (3%, 6%, etc.). This modification aims to capture the recently identified phenomenon of precipitation size reduction with increased dislocations introduced by pre-deformation (Rodgers and Prangnell, 2016; Wang et al., 2023c). An increase in dislocation (pre-deformation) can lower the energy barrier for nucleation, thus can intensify competition for the limited atoms available for precipitation growth and result a decreasing precipitate size (Dorin et al., 2014; Rodgers and Prangnell, 2016).

The stress-creep strain rate employs the hyperbolic sine function, and the sub-model is presented as:

$$\dot{\overline{\varepsilon}}^{cr} = A_3\sinh(B_1(\sigma-\sigma_{th})(1-H)^{n_2}) \tag{2–1}$$

$$\sigma_{th} = \sigma_{th_0}/(1+\exp(n_{1a}\overline{\rho}_0{}^{m_{1a}} - B)) \tag{2–2}$$

$$H = k_1(\overline{\rho}-\overline{\rho}_0) + k_2\overline{r} \tag{2–3}$$

where σ_{th} and σ_{th_0} are the creep resistance of the material caused by the dislocation-precipitate interactions, i.e. threshold stress, at the post loading and the as-received states. H is a creep variable to show the effects of microstructural evolutions of precipitates and dislocations on the macro creep deformation. n_{1a}, m_{1a}, B, A_3, B_1, n_2, k_1, k_2 are materials constants.

The material strength considers the contribution from the intrinsic strength, dislocation hardening and precipitation hardening. The sub-model is presented in Eq. (3):

$$\dot{\bar{\sigma}}_{dis} = A_2 n_d \bar{\rho}^{n_d - 1} \dot{\bar{\rho}} \tag{3–1}$$

$$\sigma_{ppt} = \left(\sigma_A{}^{-1} + \sigma_B{}^{-1}\right)^{-1} \tag{3–2}$$

$$\sigma_A = c_1^{'} \bar{r}^{m_{na}} \tag{3–3}$$

$$\sigma_B = c_2^{'} / \bar{r}^{m_{nb}} \tag{3–4}$$

$$\sigma_y = \sigma_i + \left(\sigma_{ppt}{}^{n_y} + \sigma_{dis}{}^{n_y}\right)^{1/n_y} \tag{3–5}$$

where σ_{dis} and σ_{ppt} respectively stand for the strengthening contributions of dislocations and precipitates. σ_A and σ_B respectively represent precipitation hardening variation induced by dislocation-precipitation interactions of shearing and bypassing, which have been adopted for different shaped precipitates in 2xxx and 7xxx series Al alloys (Li et al., 2017; Zheng et al., 2018). $c_1^{'}$, $c_2^{'}$, m_{na}, m_{nb}, n_d and n_y are material constants.

2.2. Transformation to anisotropic model

When considering the effect of anisotropic material strength in creep-ageing, the conventionally used isotropic Von Mises equation for describing the equivalent stress in a multiaxial state becomes inadequate. Instead, the Hill equation, also known as Hill yield criterion, is adopted to show the effect of stress state on the anisotropic plastic deformation of the material. The widely adopted Hill48 equation is given as (Cardoso and Adetoro, 2017; Lian et al., 2018)

$$\bar{\sigma}^{cr}(\boldsymbol{\sigma}) = \left(\frac{1}{2}\left(\left(F_c(\sigma_{22} - \sigma_{33})^2 + G_c(\sigma_{33} - \sigma_{11})^2 + H_c(\sigma_{11} - \sigma_{22})^2\right) + L_c\sigma_{23}^2 + M_c\sigma_{13}^2 + N_c\sigma_{12}^2\right)\right)^{\frac{1}{2}} \tag{4}$$

where $\bar{\sigma}^{cr}(\sigma)$ is the equivalent stress in the anisotropic creep-ageing scenario; σ_{ij} are the stress components of stress tensor σ; F_c, G_c, H_c, L_c, M_c, and N_c are the anisotropic coefficients for equivalent stress. For the IPA coefficients (F_c, G_c, H_c, and N_c), various forms of expressions can be adopted using the measured r-values or yield strength at 0°, 45°, and 90° (Lian et al., 2018). In this study, the IPA coefficients are expressed by referencing the previously proposed r-value-based and stress-based forms (Kawka and Makinouchi, 1996; Lian et al., 2018). The r-value-based expression is formulated as:

$$\begin{cases} \boldsymbol{F_c} = \dfrac{\boldsymbol{F_1 r_0}}{\boldsymbol{r_{90}}(1+\boldsymbol{r_0})}; \boldsymbol{G_c} = \dfrac{2}{1+\boldsymbol{r_0}} \\ \boldsymbol{H_c} = \dfrac{2\boldsymbol{r_0}}{1+\boldsymbol{r_0}}; \boldsymbol{N_c} = \dfrac{\boldsymbol{N_1}(\boldsymbol{r_{90}}+\boldsymbol{r_0})(\boldsymbol{r_{45}}+0.5)}{\boldsymbol{r_{90}}(1+\boldsymbol{r_0})} \end{cases} \tag{5}$$

where $\boldsymbol{F_1}$ and $\boldsymbol{N_1}$ are material constants to adjust the equivalent stress loci to more accurately capture the creep deformation behaviour. $\boldsymbol{r_0}$, $\boldsymbol{r_{45}}$, and $\boldsymbol{r_{90}}$ are the $\boldsymbol{r}$-values at 0°, 45°, and 90°. In the absence of $\boldsymbol{r}$-values, an alternative stress-based form can be adopted as

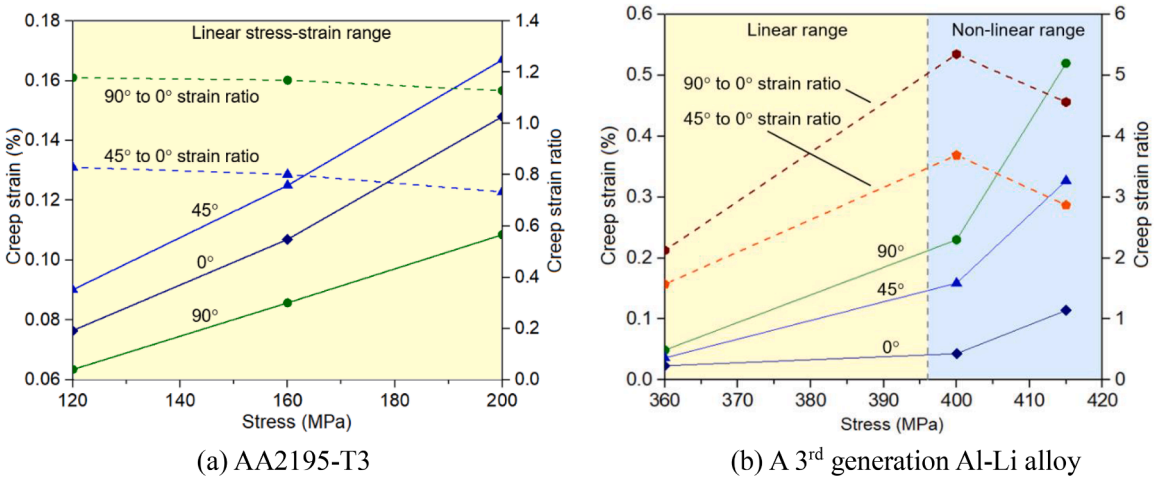

Fig. 1. Evolution of creep strains with respect to the applied stress for (a) AA2195-T3 and (b) a 3rd generation Al-Li alloy in creep-ageing. The yellow and blue regions respectively denote the stress range for the linear elastic stress-strain relation and the nonlinear stress-strain relation. The dashed lines in (a) and (b) are the creep strain ratios to the rolling direction.

follows:

$$\begin{cases} F_c = \dfrac{F_2\sigma_0^2}{\sigma_{90}^2}; G_c = 2 - \dfrac{\sigma_0^2}{\sigma_{90}^2} \\ H_c = \dfrac{\sigma_0^2}{\sigma_{90}^2}; N_c = \dfrac{N_2\sigma_0^2}{\sigma_{45}^2} - 1 \end{cases} \tag{6}$$

where F_2 and N_2 are the material constant. σ_0, σ_{45}, σ_{90} are the yield strength at 0°, 45°, and 90°. Meanwhile, for the out of plane coefficients (L_c and M_c), a value of 3 is assigned to both coefficients assuming isotropic hardening in the out of plane direction (Aretz, 2007).

It should be noted that while the Hill48 equation is well established for depicting the yielding surface and anisotropic hardening behaviour of materials, it can be inadequate for describing anisotropic creep-aging behaviour. Hence, to account for the creep anisotropy induced by the complicated grain morphology, material texture, and inhomogeneous precipitate-dislocation interactions for the as-received material when loaded at different angles to the rolling direction, a loading angle θ dependent parameter $D(\theta)$ is introduced in the stress-creep strain relation, andEq. (2–1) becomes

$$\dot{\bar{\varepsilon}}^{cr} = A_3 \sinh\{D(\theta)B_1(\bar{\sigma}^{cr}(\sigma) - \sigma_{th})(1-H)^{n_2}\} \tag{7}$$

where $\bar{\varepsilon}^{cr}$ is the equivalent creep strain in the anisotropic deformation condition. $D(\theta)$ is utilised to capture the material's anisotropic behaviour at different loading angles. Hence, it becomes crucial to properly formulate the function of $D(\theta)$ to ensure the prediction accuracy and adaptability of the model when applied to a wide range of aluminium alloys.

Fig. 1 presents a summary of experimental results for two 2xxx aluminium alloys, namely AA2195-T3 (with major weight percent (wt%) additions of 3.95 Cu, 0.32 Mg, and 0.25 Mn) and a T8 temper 3rd generation Al-Li alloy (0.6–0.9 Li, 3.4–4.5 Cu, and 0.6–1.1 Mg in wt%). It illustrates the accumulated creep strain at the end of creep-ageing with increasing applied stress at directions of 0°, 45°, and 90° to the rolling direction. It should be noted that all applied stresses for AA2195-T3 (120, 160, 200 MPa) in Fig. 1a fall within the linear elastic stress-strain relation range of the range of the material (Chen et al., 2022). In contrast, for the Al-Li alloy in Fig. 1b, the applied stress has exceeded the linear relation range with the value of σ_{end} equal to 396 MPa (Wang et al., 2022b). Fig. 1 also shows the creep strain ratios for 45° to 0° and 90° to 0°, which demonstrate monotonic decreasing or increasing in the elastic regions.

The anisotropic deformation behaviour can be observed from Fig. 1 when creep-ageing is performed at different angles for different alloys. This anisotropic creep behaviour has been well identified as the result of complex interactions among grain morphology, material texture, and inhomogeneous precipitate-dislocation effects (Chen et al., 2022; Wang et al., 2023c). On the other hand, for each of the alloy, the creep strain ratios of 45° and 90° to the rolling direction exhibit different evolution rates with increasing stress. This indicates varying anisotropy evolution with higher applied stress in creep-ageing for different directions. The difference in anisotropy evolution with increasing stress at varying directions in creep-ageing can be attributed to the combined effects of the as-received material texture and the activation of corresponding non-octahedral slip systems at higher applied stress, which can be more beneficial for creep deformation at specific loading angles and lead to the creep strain ratio evolution with varying rates (Li et al., 2021). Hence, to consider the material-induced anisotropy as well as its dynamic effect on creep deformation with varying stress applied in creep-ageing, $D(\theta)$ is formulated in the following equation to extend the rolling-direction based material model to an anisotropic one as

$$D(\theta) = 1 + \beta(\theta)\tanh(\langle\sigma - \sigma_{th0}\rangle^{n_3}/C_1) \tag{8}$$

where $\beta(\theta)$ is a function of θ constructed using NURBS to capture the material-induced anisotropic behaviour across different loading directions. NURBS is widely adopted as mathematical tool capable of constructing smooth continuous curve based on a limited set of determined points on the coordinate axis. The algorithm and application of NURBS to construct nonconstant anisotropic coefficients as a function of θ were specifically illustrated in (Cardoso and Adetoro, 2017). It should be noted that $\beta(0°)$ is equivalent to the value of 0, thus the anisotropic material model becomes its original rolling direction based form. A monotonic tanh equation is employed to capture the dynamic creep deformation anisotropy evolution with increasing stress at specific loading angle. n_3, C_1 in Eq. (8) are material constants. The $\langle\ \rangle$ is Macaulay brackets, adopted to return a value of 0 when $\sigma < \sigma_{th0}$ (σ_{th0} is the initial threshold stress below which creep deformation cannot be initiated). The adopted tanh equation is particularly suited for describing the creep deformation anisotropy evolution trend: the evolution initially intensifies with higher applied stress due to the activation of certain non-octahedral slip systems at specific loading angles; however, with further increasing stress, it will gradually reduce due to the accumulation of dislocations which can act as strong hinderances to the movement (Li et al., 2023a; Wang et al., 2023c). Thus, by using the NURBS function $\beta(\theta)$ and an applied stress dependent tanh equation, $D(\theta)$ becomes a loading angle dependent parameter that not only captures the effects of material induced anisotropy on creep deformation, but also reflects its varying trend with different applied stress in creep-ageing.

Additionally, a sharp turn in the creep strain ratios can be observed in Fig. 1b in the nonlinear range. This sharp turn in anisotropy evolution trend can be attributed to the rapid increase of dislocations introduced by larger creep deformation in the nonlinear loading range and the resulting stronger hinderance caused by the pinning and pileups in the dislocation-precipitate interactions (Li et al., 2023a; Wang et al., 2023c). In order to capture the abrupt shift in the evolution trend of the creep anisotropy in the non-linear stress-strain range, $D(\theta)$ is further extended as

$$\begin{cases} D(\theta) = 1 + \beta(\theta)\tanh(\langle\sigma - \sigma_{th0}\rangle^{n_3}/C_1)/\gamma(\sigma) \\ \gamma(\sigma) = \exp(\langle\sigma_{th_0} - \sigma_{th}\rangle/C_2) \end{cases} \tag{9}$$

where $\gamma(\sigma)$ takes into consideration of the increased dislocation-precipitate hinderance to creep deformation at all directions in the non-linear stress-strain range when σ surpasses σ_{end}. It is worthing noting that with the use of Macaulay brackets, Eq. (9) remains consistent with Eq. (8) in the elastic stress range when $\sigma < \sigma_{end}$. C_2 in Eq. (9) is a material constant.

2.3. Anisotropic model for materials with pre-deformation

Introducing more mobile dislocations through pre-deformation (PD) has been shown to be an effective treatment to enhance the formability for high strength aluminium alloys during creep-ageing (Li et al., 2021; Rong et al., 2019). On the other hand, the additional dislocations introduced by PD can alter both the long and short range internal stresses during plastic deformation, thus exerting significant impact on the anisotropic creep deformation behaviour of the material (Chen et al., 2022; Peng et al., 2022). The variation of long range stress can be attributed to the reconfiguration of dislocation substructures, while the evolution of the short range stress is the result of the precipitation of the major strengthening θ' and T_1 precipitates for the 2xxx Al-Cu and Al-Li alloys (Chen et al., 2022). In addition, when compared to the strong effects exerted by texture on material anisotropy in the as-received state such as in T3 and T8 tempers (Chen et al., 2020; Xu et al., 2018), recent studies also highlighted the dominance of dislocation cell (DC) morphology evolution over the material texture in influencing the anisotropy of creep deformation and strength of the material (Chen et al., 2022; Wang et al., 2023c).

During creep deformation, the long range internal stress (τ_l) that contributes to creep resistance can be expressed as (Thompson, 1977):

$$\tau_l = \alpha G b l^{-m} \tag{10}$$

where G and b are respectively the shear modulus and the magnitude of the burgers vector, l is the length of the DC structure, α and m are material constants.

To evaluate the change of l with pre-deformation in the anisotropic scenario, a normalised DC length $\bar{l}_\theta$ is defined as:

$$\bar{l}_\theta = \frac{l_\theta}{l_{0^\circ}^{ref}} \tag{11}$$

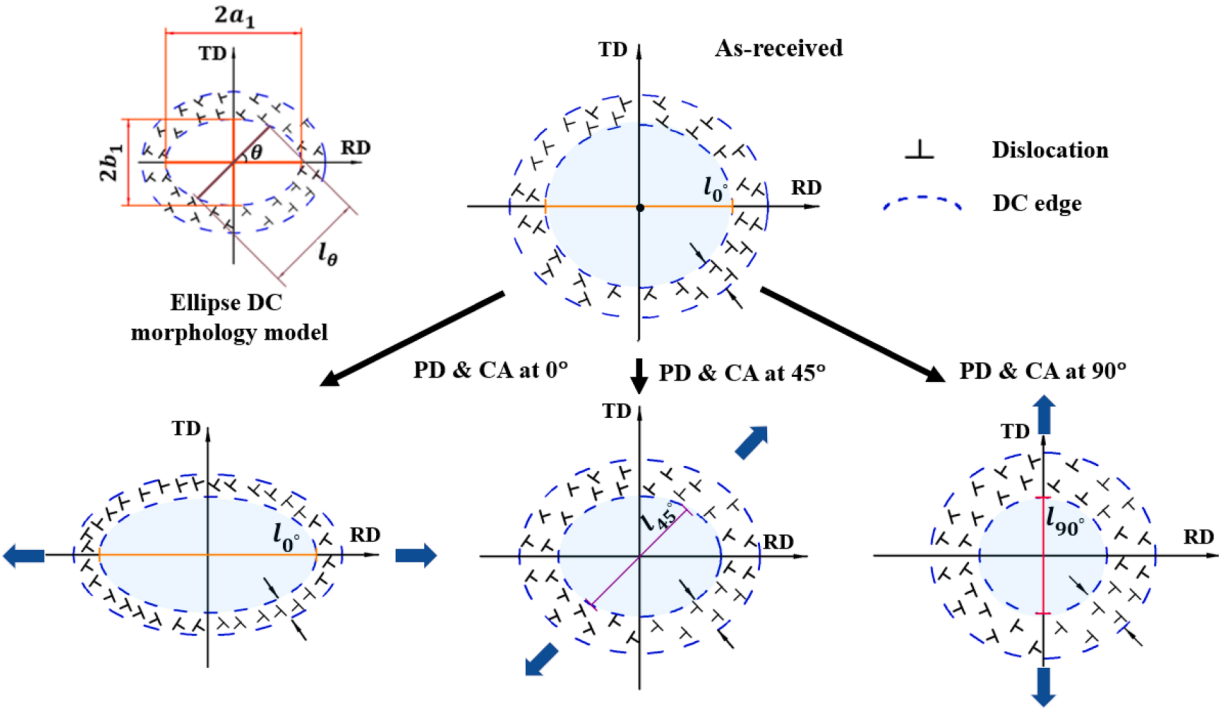

Fig. 2. Schematic of ellipse dislocation cell (DC) morphology and its evolution with PD and creep-ageing at the same directions along 0°, 45°, and 90° to the rolling direction. PD & CA refers to pre-deformation and creep-ageing. $\boldsymbol{l_\theta}$ denotes the DC length at angle $\boldsymbol{\theta}$ to the rolling direction.

where l_θ is the DC length at angle θ to the rolling direction and $l_{0^\circ}^{\mathrm{ref}}$ represents the value of l_θ at the rolling direction as the reference. By definition, $\bar{l}_{0^\circ} = 1$. When reconfiguration of DC occurs with PD and creep-ageing, the variation of long range internal stress $\Delta\tau_l$ can be further derived as:

$$\Delta\tau_l = \alpha G b l_{0^\circ}^{ref\,-m}(\bar{l}_\theta^{\,-m} - \bar{l}_{0^\circ}^{\,-m}) = g(\bar{l}_\theta^{\,-m} - 1) \tag{12}$$

where g is employed for simplification to replace the term $\alpha G b l_{0^\circ}^{\mathrm{ref}\,-m}$.

When plastic deformation occurs, the processes of dislocation generation, remobilisation, as well as annihilation are induced simultaneously to accommodate the deformation of the material, leading to the morphology evolution of the dislocation cells (Dannoshita et al., 2022; Farid et al., 2021). Fig. 2 schematically summarises the observed ellipse DC model and evolutions of DC morphology with 6% PD and creep-ageing along the same direction at 0°, 45°, and 90° in (Wang et al., 2023c). As shown in Fig. 2, the investigation found that elongated DCs are induced when the as-received material undergoes 6% PD and creep-ageing at the rolling direction. While when the material undergoes the same treatments at 45° and 90° directions, DCs with smaller sizes and widened edges are observed (Wang et al., 2023c).

Two cases are included in the framework as follows: (1) PD and creep-ageing at the same angle $\boldsymbol{\theta}$ to the rolling direction; (2) Unidirectional PD treatment followed by creep-ageing at various directions. To express the DC morphology evolution with PD treatment, the length of DC (l_θ) can be related to the local dislocation density (ρ_{DC}) as (Holt, 1970):

$$l_\theta = k \Big/ \sqrt{\rho_{DC}} \tag{13}$$

where k is a material constant. Additionally, the dislocation evolution within the DC has the following kinetic relationship with the macro deformation (Roters et al., 2000; Viatkina et al., 2007):

$$\dot{\rho}_{DC} = \frac{MI}{b}\sqrt{\rho_{DC}}\dot{\varepsilon} - \dot{\rho}_{DC}^{\mathrm{remob}} - \dot{\rho}_{DC}^{\mathrm{ann}} \tag{14}$$

where ε is the macro deformation strain. The first term accounts for the stored mobile dislocations in the DC. $\rho_{DC}^{\mathrm{remob}}$ and ρ_{DC}^{ann} represent respectively the dislocation density reduction induced by remobilisation and annihilation. M and I are material constants for the Taylor factor and effective slip length. In the scenario of monotonic deformation at constant loading direction, the contributions of $\rho_{DC}^{\mathrm{remob}}$ and ρ_{DC}^{ann} can be calculated as $\dot{\rho}_{DC}^{\mathrm{ann}} + \dot{\rho}_{DC}^{\mathrm{remob}} = \frac{M}{b}R_1\rho_{DC}\dot{\varepsilon}$(Viatkina et al., 2007), where R_1 is a material constant. Hence, Eq. (14) can be further written to describe the dislocation evolution in the monotonic deformation process as

$$\dot{\rho}_{DC} = \frac{M}{b}\left(I\sqrt{\rho_{DC}} - R_1\rho_{DC}\right)\dot{\varepsilon} \tag{15}$$

On the other hand, under nonmonotonic deformation, changes in loading direction and the corresponding strain path can alter the size and morphology of DCs (Clausmeyer et al., 2013; Kida et al., 1997; Sakharova and Fernandes, 2006). With changes in the strain path, the reconfiguration of DC can involve various processes such as dislocation migration, splitting and reorganisation (Pinheiro et al., 2004; Wejdemann et al., 2013). These rearrangements can form immobilised dislocation structures which can lead to DC splitting and forming of new sub-boundaries (Kida et al., 1997; Wejdemann et al., 2013). As a result, smaller sized DCs are observed after the dislocation rearrangement process as reported in (Kida et al., 1997; Wejdemann et al., 2013). To more accurately express the correlation between the dislocation evolution and the change in loading direction, by referencing the structure of Eq. (15), the kinetic relation between the evolutions of strain and dislocation density of a DC in nonmonotonic deformation is written as

$$\dot{\rho}_{DC} = \frac{M}{b}\left(I\sqrt{\rho_{DC}} - R_1\rho_{DC}\right)\dot{\varepsilon} + \frac{M}{b}I\mu_\theta\sqrt{\rho_{DC}}\dot{\varepsilon} = \frac{M}{b}\left((1+\mu_\theta)I\sqrt{\rho_{DC}} - R_1\rho_{DC}\right)\dot{\varepsilon} \tag{16}$$

where the second term $\frac{M}{b}I\mu_\theta\sqrt{\rho_{DC}}\dot{\varepsilon}$ is introduced to characterise the dislocation density variation caused by nonmonotonic deformation. μ_θ is a loading angle dependent parameter as a function of θ to express the anisotropy of dislocation variation within a DC when deformed along different directions. Combining Eqs. (11), (13), and (16), the relation between te normalised DC length and material deformation can be derived as

$$\dot{\bar{l}}_\theta = \frac{M}{2b}\left(R_1\bar{l}_\theta - -(1+\mu_\theta)Ik^{-1}l_{0^\circ}^{\mathrm{ref}}\bar{l}_\theta^{-2}\right)\dot{\varepsilon} = \left(k_3\bar{l}_\theta - k_4(1+\mu(\theta))\bar{l}_\theta^{-2}\right)\dot{\varepsilon} \tag{17}$$

where $k_3 = R_1M/2b$ and $k_4 = IMk^{-1}l_{0^\circ}^{\mathrm{ref}}/2b$. With Eqs. (12) and (17), the constitutive relation between macro PD and microstructure DC length variation, as well as their impact on the anisotropic creep deformation behaviour with PD can be reflected.

In the second case, the material has undergone uniform PD treatment as the as-received state, the long range internal stress can vary in the subsequent creep-ageing at various directions, due to the difference of l_θ in the deformed DC at different angle θ to the rolling direction. This variation of long range internal stress can cause anisotropic behaviour when creep-aged at different directions after PD (Chen et al., 2022). Considering the eclipsed morphology DC model as illustrated in Fig. 2, l_θ can be calculated using the geometric relationship as

$$l_\theta = 2a_1 b_1 \left(b_1{}^2 cos^2\theta + a_1{}^2 sin^2\theta\right)^{-1/2} \tag{18}$$

Combining with Eq. (11) and $l_{0^\circ}^{\mathrm{ref}} = 2a_1$, the normalised DC length can be calculated as

$$\overline{l_\theta} = \frac{l_\theta}{l_{0^\circ}^{ref}} = b_1 \left(b_1{}^2 cos^2\theta + a_1{}^2 sin^2\theta\right)^{-1/2} \tag{19}$$

For the precipitation evolution of Al-Cu and Al-Li alloys with PD treatment and creep-ageing at various angles to the rolling direction, no significant differences of the evolution of θ' and T_1 precipitates were observed between different directions (Chen et al., 2022; Peng et al., 2022). Hence, the effect of short-range stress induced by precipitation-dislocation interaction can be included in the same form regardless of the loading direction. The term $(1 + \gamma_0 \overline{\rho}^{m_4})$ in Eq. (1–4) captures the effect of precipitation promotion with increased dislocation density, while the effect of the precipitate and dislocation evolutions on creep deformation are accounted for by introducing the variable H in Eq. (2–1) (Li et al., 2017; Wang et al., 2022b, 2022a). Correspondingly, the stress-creep strain relation Eq. (7) can be rewritten at PD condition by incorporating the long range internal stress change $\Delta_{\tau l}$:

$$\dot{\overline{\varepsilon}}^{cr} = A_3 \sinh(D(\theta) B_1 (\overline{\sigma}^{cr}(\sigma) - \sigma_{th} - \Delta\tau_l)(1 - H)^{n_2}) \tag{20}$$

2.4. Anisotropic model for material strength

An index known as in-plane anisotropy (IPA) is widely accepted and used to quantitatively evaluate the extent of the observed anisotropy including creep deformation and material strength. IPA is calculated as

$$IPA = \frac{2X_{max} - X_{mid} - X_{min}}{2X_{max}} \tag{21}$$

where X_{max}, X_{mid}, and X_{min} represent the maximum, mid, and minimum values of the experimental results (creep deformation or strength) obtained under the same condition at the directions of 0°, 45°, and 90°. Based on the definition of IPA, this index ranges from 0 to 1, with larger values signifying the increased level of material anisotropy. Fig. 3a presents the summary results of yield strength IPA evolutions for various 2xxx aluminium alloys during creep-ageing, including AA2219-T3 creep-aged under 120 MPA (Chen et al., 2020), AA2524-T3 creep-aged under stress range from 120 to 150 MPa (Xu et al., 2018), and T8 temper Al-Li alloy creep-aged with different PD extent from 0% to 6% (Wang et al., 2023c).

From the summarised results in Fig. 3a, a reduction of strength IPA can be observed with creep-ageing under various conditions for different 2xxx aluminium alloys. Fig. 3b shows the strength IPA reduction in comparison with their as-received states. The strength IPA reduction (I_R) is calculated using the equation as $I_R = (IPA_0 - IPA_t)/IPA_0$, where IPA_0 and IPA_t represent the IPA values obtained at the as-received state and after creep-ageing for time t under the same experiment conditions. As shown in Fig. 3b, a maximum IPA reduction of 93% is induced for AA2219-T3 after creep-ageing at 120 MPa for 6 h. In addition, Fig. 3b illustrates an enhancement of the reduction in strength IPA with varying of conditions including increasing creep-ageing time, PD extents, and stress level. Previous investigations attributed the reduction in material strength anisotropy during creep-ageing to the enhanced evolution of plate-shaped

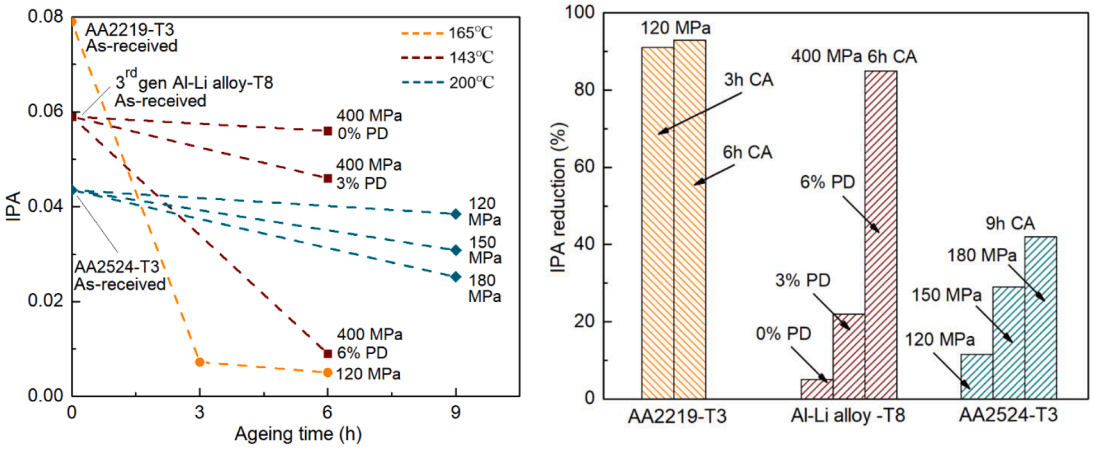

(a) Strength IPA evolution (b) Strength IPA reduction

Fig. 3. Evolution and reduction of yield strength IPA for different 2xxx aluminium alloys with creep-ageing. (a) demonstrates the IPA evolution of AA2219-T3 creep-aged at 120 MPa and 165 °C, T8 temper 3rd generation Al-Li alloy with different extents of tensile pre-deformation from 0% to 6% creep-aged at 400 MPa and 143 °C, and T3 temper AA2524 creep-aged at different stresses from 120 MPa to 180 MPa under 200 °C. (b) presents the IPA reduction for different alloys at varying conditions in creep-ageing in comparison to their as-received states.

major strengthening precipitates, such as T_1 and θ', on the {111} and {110} habit planes as well as the corresponding stress orientation-independent dislocation hardening effects. These effects can balance the critical resolved shear stress (CRSS) across varying loading directions, and thus diminishing the crystallographic texture induced strength anisotropy in the as-received material with the progresses of creep-ageing (Chen et al., 2020; Wang et al., 2023c). Consequentially, an enhancement in anisotropy reduction can be induced by the promotion in precipitation and dislocation density due to increased creep-ageing time, stress level, and PD treatments.

Considering the diminishing effect on the strength anisotropy of the as-received material with proceeding of creep-ageing, the material yield strength evolution Eq. (3–5) are modified by introducing $\alpha_d(t,\theta)$ as

$$\begin{cases} \sigma_i(t,\theta) = \alpha_d(t,\theta)\sigma_i \\ \alpha_d(t,\theta) = (1-\alpha(\theta)(1-\tanh(t/\alpha_1))) \end{cases} \tag{22–1}$$

$$\sigma_y = \sigma_i(t,\theta) + \left({\sigma_{ppt}}^{n_y} + {\sigma_{dis}}^{n_y}\right)^{1/n_y} \tag{22–2}$$

where $\alpha_d(t,\theta)$ is a strength anisotropy diminishing parameter which is dependent on creep-ageing time and loading angle. This parameter is introduced to reflect the diminishing effect on strength anisotropy at different directions with the proceeding of creep-ageing. This parameter consists of a NURBS function of $\alpha(\theta)$ and a tanh equation, where the former is employed to express the strength anisotropy of the as-received material, and the latter describes the anisotropy reduction with proceeding of creep-ageing. When $t = 0$, $\alpha_d(\theta)$ shows the anisotropy of material strength in the as-received state induced by the complex inherited factors such as the grain morphology and crystallographic texture in the material. Additionally, the monotonic tanh function has a value range between 0 and 1, the term $1 - \tanh(t/\alpha_1)$ in Eq. (22–1) is capable of capturing the diminishing trend of initial material strength anisotropy as creep-ageing time t increases. α_1 in the tanh function is a material constant.

With the above equations, the anisotropic creep-ageing behaviour for various 2xxx series Al alloys at the as-received and pre-deformed states can be captured. The key equations employed in this framework are summarised in Table 1.

It is noted that there is potential to extend the proposed framework to 7xxx series aluminium alloys. However, the anisotropic creep-aging behaviour of 7xxx series aluminium alloys has rarely been investigated, possibly because of their less significant anisotropy. Consequently, the feasibility of the proposed framework for 7xxx series aluminium alloys needs further verification.

2.5. Model calibration and implementation

For calibration of the model, the experimentally obtained uniaxial creep-ageing test results at different angles to the rolling di-

Table 1
Equations to capture anisotropic creep deformation and strengthening for 2xxx series Al alloys in the proposed framework.

Key equations employed for anisotropic creep deformation	
$\overline{\sigma}^{cr}(\boldsymbol{\sigma}) = \left(\frac{1}{2}\left(\left(F_c(\sigma_{22}-\sigma_{33})^2 + G_c(\sigma_{33}-\sigma_{11})^2 + H_c(\sigma_{11}-\sigma_{22})^2\right) + L_c\sigma_{23}^2 + M_c\sigma_{13}^2 + N_c\sigma_{12}^2\right)\right)^{\frac{1}{2}}$ (4)	
$\dot{\overline{\rho}} = A_1(1-\overline{\rho})\lvert\dot{\overline{\varepsilon}}^{cr}\rvert^{m_1} - C_p\overline{\rho}^{m_2}\lvert\dot{\overline{\varepsilon}}^{cr}\rvert^{m_5}$ (1–3)	
$\dot{\overline{r}} = C_r(Q-\overline{r})^{m_3}(1+\gamma_0\overline{\rho}^{m_4})$ (1–4)	
$\dot{\overline{\varepsilon}}^{cr} = A_3\sinh(D(\theta)B_1(\overline{\sigma}^{cr}(\boldsymbol{\sigma}) - \sigma_{th} - \Delta\tau_l)(1-H)^{n_2})$ (7)	
$\overline{\sigma}^{cr}(\boldsymbol{\sigma})$: Equivalent stress; σ_{11}, σ_{22}, σ_{33}, σ_{12}, σ_{13}, σ_{23}: Stress components; $\overline{\rho}$: Normalised dislocation density; $\overline{\varepsilon}^{cr}$: Equivalent creep strain; $\overline{r}$: Normalised precipitate size; $D(\theta)$: Loading angle dependent parameter for anisotropic deformation; $\overline{\sigma}_{cr}(\boldsymbol{\sigma})$: Equivalent stress in the anisotropic creep-ageing σ_{th}: Threshold stress in creep-ageing; $\Delta\tau_l$: Variation in long range internal stress; H: Creep variable.	$F_c, G_c, H_c, L_c, M_c, N_c, A_1, m_1, C_p, m_2, m_5, C_r, m_3, \gamma_0, m_4, A_3, B_1, n_2$ are material constants.
Key equations employed for anisotropic strengthening	
$\dot{\sigma}_{dis} = A_2 n_d \overline{\rho}^{n_d-1}\dot{\overline{\rho}}$ (3–1)	
$\sigma_{ppt} = \left({\sigma_A}^{-1} + {\sigma_B}^{-1}\right)^{-1}$ (3–2)	
$\sigma_i(t,\theta) = \alpha_d(t,\theta)\sigma_i$ (22–1)	
$\sigma_y = \sigma_i(t,\theta) + \left({\sigma_{ppt}}^{n_y} + {\sigma_{dis}}^{n_y}\right)^{1/n_y}$ (22–2)	
σ_{dis}: Dislocation hardening; σ_{ppt} : Precipitation hardening; σ_A: Strengthening by dislocation cutting through precipitates; σ_B: Strengthening by dislocation bypassing precipitates; $\alpha_d(t,\theta)$: Coefficient to express the strength anisotropy diminishing effect with creep-ageing; σ_i: Intrinsic strength; σ_y: Yield strength.	A_2, n_d, n_y are material constants.

rection are utilised. By employing the load transformation to decompose the applied uniaxial stress σ into its components along the rolling, transvers, and normal directions (represented with 1, 2 and 3 respectively), the stress components can be derived as

$$\begin{cases} \sigma_{11} = \cos^2(\theta)\sigma \\ \sigma_{22} = \sin^2(\theta)\sigma \\ \sigma_{12} = -\cos(\theta)\sin(\theta)\sigma \\ \sigma_{33} = \sigma_{13} = \sigma_{23} = 0 \end{cases} \tag{23}$$

The equivalent stress $\overline{\sigma}^{cr}(\boldsymbol{\sigma})$ in Eq. (4) can be expressed using the stress components in Eq. (23) as

$$\overline{\sigma}^{cr}(\boldsymbol{\sigma}) = \left(\frac{1}{2}\left(\left(F_c\sin^4(\theta) + G_c\cos^4(\theta) + H_c\left(\cos^2(\theta) - \sin^2(\theta)\right)^2\right)\sigma^2 + N_c\cos^2(\theta)\sin^2(\theta)\sigma\right)\right)^{\frac{1}{2}} \tag{24}$$

By incorporating $\overline{\sigma}^{cr}(\boldsymbol{\sigma})$ into Eq. (20), the equivalent creep strain rate $\dot{\overline{\varepsilon}}_{cr}$ can be obtained. The equivalent creep strain increment is $\mathrm{d}\overline{\varepsilon}^{cr} = \dot{\overline{\varepsilon}}^{cr}\Delta t$, where Δt is the time increment. By applying the flow rule, the strain increment in each direction is calculated as

$$d\varepsilon_{ij}^{cr} = d\overline{\varepsilon}^{cr}\frac{\partial\overline{\sigma}_{cr}(\sigma)}{\partial\sigma_{ij}} \tag{25}$$

where $\mathrm{d}\varepsilon_{ij}^{cr}$ are the components of creep strain increment $\mathrm{d}\overline{\varepsilon}^{cr}$. The creep strain increment at the loading direction $\mathrm{d}\varepsilon^{cr}$ can be formulated as

$$\mathrm{d}\varepsilon^{cr} = \cos^2(\theta)d\varepsilon_{11}^{cr} + \sin^2(\theta)d\varepsilon_{22}^{cr} - \sin(2\theta)d\varepsilon_{12}^{cr} \tag{26}$$

Correspondingly, the creep strain at loading direction, which is equivalent to the measured value during the uniaxial creep-ageing test, can be calculated as $\varepsilon^{cr} = \int \mathrm{d}\varepsilon^{cr}$. With the fitted and measured value of ε_{cr}, by employing the well-developed combined forward Euler and the least square methods (Li et al., 2017; Wang et al., 2022b), the material constants can be calibrated to yield good results.

For implementing the model into numerical simulation, with the calculated creep strain increment components, the variation of stress components induced by creep deformation at each iteration step is updated as

$$\begin{cases} \mathrm{d}\sigma_{ij} = \boldsymbol{C_e}\left(\mathrm{d}\varepsilon_{ij} - \mathrm{d}\varepsilon_{ij}^{cr}\right) \\ \boldsymbol{\sigma}' = \boldsymbol{\sigma} + \Delta\boldsymbol{\sigma} \end{cases} \tag{27}$$

where $\mathrm{d}\sigma_{ij}$ represents the increment of the stress components, $\boldsymbol{C_e}$ is the elasticity stiffness tensor, $\boldsymbol{\sigma}'$ and $\boldsymbol{\sigma}$ are respectively the updated and original stress states at the beginning of the iteration, and $\boldsymbol{\Delta\sigma}$ is the stress increment tensor of $\mathrm{d}\sigma_{ij}$. It is noteworthy that by following the above calibration and implementation procedures, the model can guarantee the consistency of its predicted values in the anisotropic scenario at the loading, rolling, transverse, and normal directions of the material.

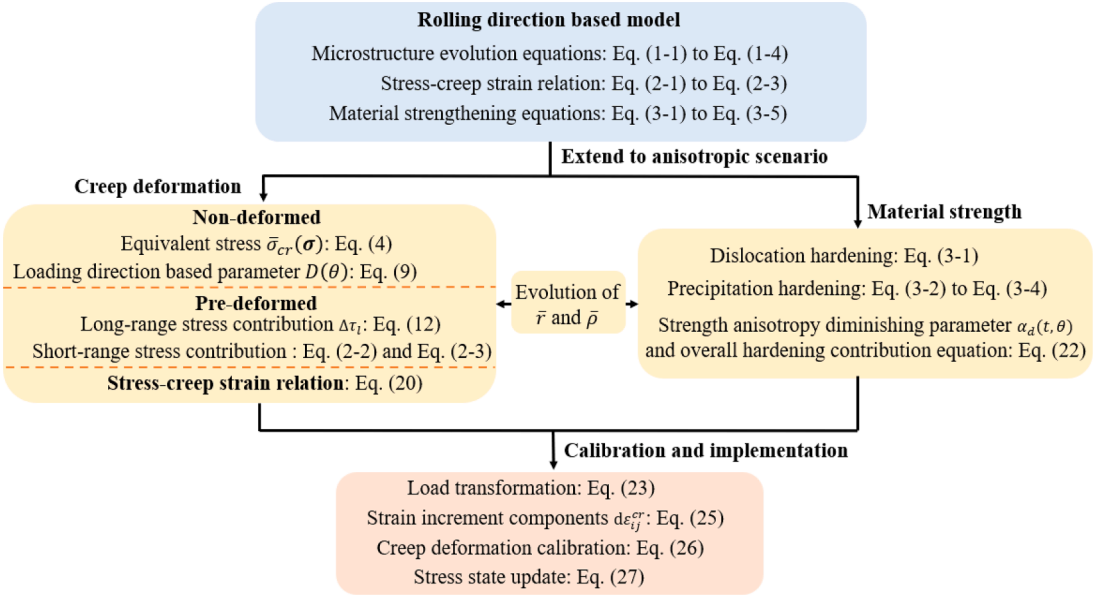

Fig. 4. Proposed routine for establishing an anisotropic model as well as its calibration and implementation.

Fig. 4 summarises the routine for establishing an anisotropic model as well as its calibration and implementation. The evolution of precipitation and dislocation is a key link between the creep deformation and material strength.

It is noted that more parameters are employed in the proposed generalised model than in the original rolling direction based isotropic material model. The newly introduced parameters are the key to extending the original rolling direction model into a generalised framework which can describe the complex anisotropic deformation and strengthening behaviours of various 2xxx series aluminium alloys with and without pre-deformation. The introduced parameters not only help to construct the generalised framework but also provide more robustness in describing the anisotropic behaviours of 2xxx series aluminium alloys in creep-ageing, where these behaviours can vary significantly as demonstrated in this and previous studies.

Furthermore, it is acknowledged that most of the newly introduced parameters in this work are proposed based on generalised microstructural evolutions that can explain the observed macro anisotropic creep ageing behaviours for various 2xxx series aluminium alloys, rather than addressing each specific physical factor individually. This is because that in the complex anisotropic scenario where various micro scale factors can affect the macro deformation behaviour in creep-ageing, a much greater number of parameters with specific physical meanings (such as the volume fractions of material textures, the number of slip systems activated at specific loading angle and stress levels, etc.) would be needed to address the changes. This would substantially increase the experimental work, make the data fitting process more challenging, and complicate the implementation of the model for processing simulation.

3. Model validation and application

This section provides validation examples of anisotropic model establishment utilising experimental results of anisotropic creep deformation and age hardening behaviours of various 2xxx aluminium alloys including 3rd generation Al-Li alloy, as well as AA2195 and AA2219 in various tempers. Furthermore, the anisotropic behaviours during creep-ageing of both the 3rd generation Al-Li alloy and AA2219, which had undergone different PD treatments, are included for verification. The material constants are determined using the widely adopted forward Euler method and the least square method. The methods employed to determine the material constants, as well as the summary of the obtained material constant values are further illustrated in Appendix A.

3.1. Validation for the creep deformation prediction

3.1.1. T3 temper AA2195

The anisotropic uniaxial creep deformation behaviour of AA2195-T3 at 0°, 45° and 90° was investigated at 180 °C under the stress levels of 120, 160, and 200 MPa in (Peng et al., 2022). The applied stresses did not surpasses the linear elastic region of the material as they were significantly lower than the yield strength at the rolling direction (281 MPa) (Peng et al., 2022). As a result, $\langle \sigma - \sigma_{end} \rangle = 0$ and $\gamma(\sigma) = 1$, thus Eq. (9) reverts back to Eq. (8). The threshold stress σ_{th0} in Eq. (10) is determined to be 60 MPa, using a routine proposed in (Wang et al., 2022b), which is further illustrated in Appendix B.

The equivalent stress can be calculated using Eq.(24). Furthermore, with the anisotropic yield stresses at 0°, 45° and 90°, i.e. σ_0, σ_{45}, and σ_{90}, reported in (Peng et al., 2022), the stress-based anisotropic coefficients in Eq. (6) are utilised. The employed equations as well as the determined values of the material constants and anisotropic parameters for establishing the AA2195-T3 model are listed in Table 2.

The values of material constants and anisotropic parameters $\beta(\theta)$ are listed in Table 2. The monotonically decreasing NURBS curve of $\beta(\theta)$ is shown in Fig. 5a, as well as the curve of $D(\theta)$ obtained using Eq. (8). Fig. 5b to 5d demonstrate the creep deformation prediction results using the established NURBS curves for 0°, 45° and 90° directions under the stress levels of 120, 160 and 200 MPa. It can be observed that satisfying agreements with the experimental results are achieved for the creep deformation at 0°, 45° and 90° under varying stresses.

Table 2
Employed equations, determined material constants and anisotropic parameters for the AA2195-T3 model.

Employed equations							
Equivalent stress: Eq. (24) Stress-creep strain relation: Eq. (7);					Microstructural evolution: Eqs. (1–1) to (1–4); Model calibration: Eqs. (23) to (26);		
Anisotropic yield stresses (Peng et al., 2022)							
σ_0 (MPa) 281		σ_{45} (MPa) 245			σ_{90} (MPa) 269		
Material constants and anisotropic parameters determined in this study							
A_1 (h^{-1})	A_3 (h^{-1})	B_1 (MPa^{-1})	C_1	C_p	C_r (h^{-1})	F_2	k_1
20	6.9E-5	2.5E-2	70	1.5E-3	6E-2	0.68	0.5
k_2	m_1	m_2	m_3	m_4	N_2	n_2	n_3
2.5E-4	0.482	0.95	1.36	1.5	2.6	3.9	1
Q	$\beta(0^*)$	$\beta(45^*)$	$\beta(90^*)$	γ_0	σ_{th0} (MPa)		
0.68	0	−0.13	−0.145	8	11		

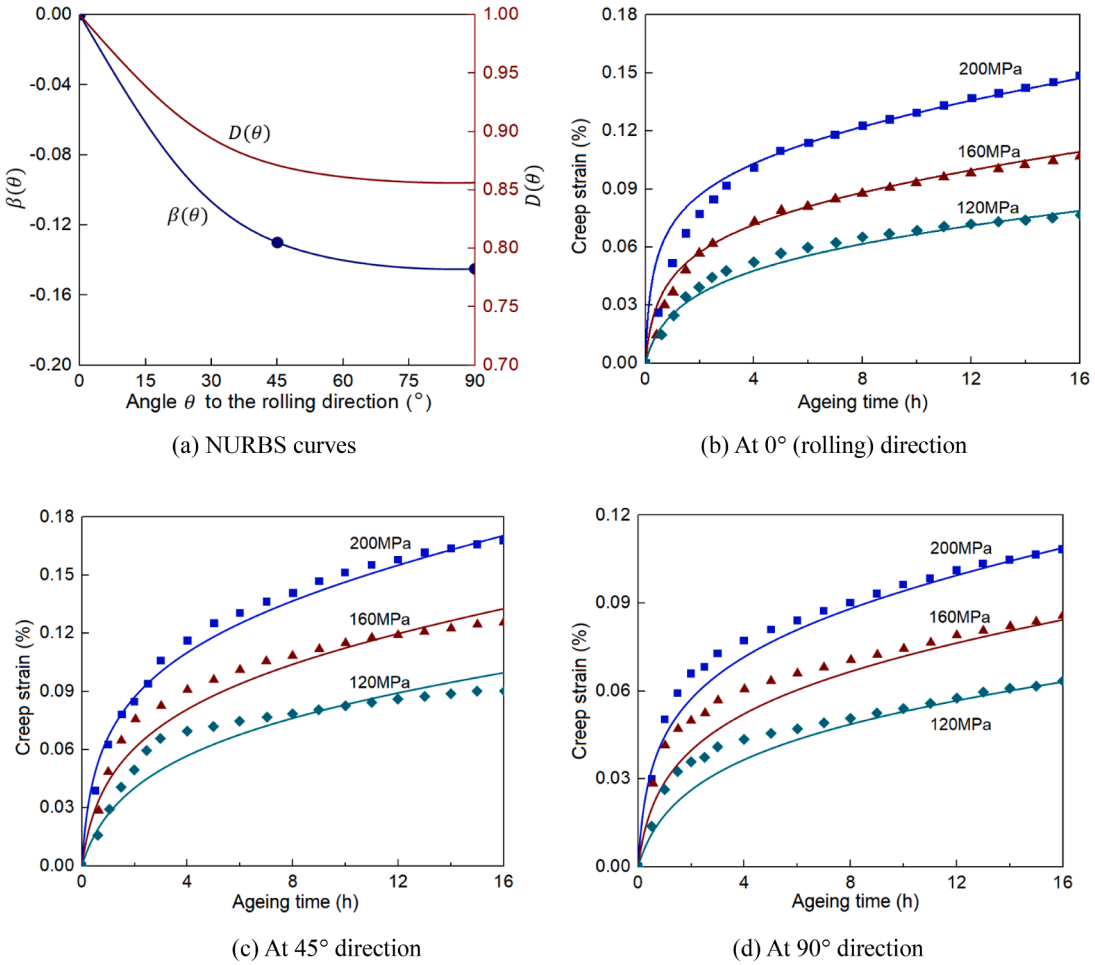

Fig. 5. NURBS curves of $\boldsymbol{\beta}(\boldsymbol{\theta})$ and $\boldsymbol{D}(\boldsymbol{\theta})$ at 160 MPa, and comparison of the prediction (lines) and experimental (symbols) results for AA2195-T3 creep-aged at 180 °C at indicated stress levels for different loading directions.

Table 3
Employed equations, determined material constants and anisotropic parameters for the as-received 3rd generation Al-Li alloy.

Employed equations						
Equivalent stress: Eq. (24); Stress-creep strain relation: Eq. (7);			Microstructural evolutions: Eqs. (1–1) to (1–4); Model calibration: Eqs. (23) to Eq. (26);			
Materials properties from (Wang et al., 2023b)						
r_0	r_{45}		r_{90}		σ_{end} (MPa)	
0.96	0.52		1.49		396	
Material constants determined in (Wang et al., 2022b)						
A_1 (h^{-1})	A_3 (h^{-1})	B	B_1 (MPa^{-1})	C_p	C_r (h^{-1})	E (MPa)
26	8.43E-8	10.5	3.6E-2	6.5E-3	8E-2	6.98E4
E' (MPa)	K (MPa^{-1})	k_1	k_2	m_1	m_{1a}	m_2
6.26E4	9.36E-8	0.5	5.2E-2	0.542	0.52	0.75
m_3	m_4	n_2	n_{1a} Q	γ_0	σ_{th_0}(MPa)	m_5
1.05	1.5	1.28	50 1.52	8	105	1
Material constants and anisotropic parameters determined in this study						
C_1	C_2	F_1	m_5	m_6	N_1	n_3
2E16	100	3.6	1	1	3	6.5
$\beta(0°)$	$\beta(15°)$	$\beta(45°)$	$\beta(90°)$			
0	0.22	0.38	0.51			

3.1.2. T8 temper 3rd generation Al-Li alloy (0.6 to 0.9 wt.% Li)

A T8 temper 3rd generation Al-Li alloy was creep-aged in directions ranging from 0° to 90° at 143 °C and under the stresses of 360 MPa, 400 MPa, and 415 MPa (Wang et al., 2023b). The applied stress of 415 MPa surpasses upper limit of 396 MPa for the linear stress-strain relation of the material, hence $\gamma\ (\sigma)$ in Eq. (9) is no longer equal to 1. Table 3 demonstrates the equations used for the model and the values of the material constants and anisotropic parameters.

Fig. 6a demonstrates the NURBS curve of $\beta(\theta)$ and the evolution curve of $D(\theta)$ correspondingly determined from Eq. (9). It can be observed that a smooth monotonically increasing curve is established with fitted values of $\beta(\theta)$ at 0°, 15°, 45° and 90°. Also, a dynamic variation of $D(\theta)$ with varying loading angle can be observed. By utilising the established NURBS curves shown in Fig. 6a, the strong anisotropic behaviour, characterised by a 5 times increase of creep deformation from 0° to 90° when creep-aged at 415 MPa for 6 h, is adequately captured, as demonstrated by the prediction results in Fig. 6b to 6d. On the other hand, the creep deformation under different stresses of 360 to 415 MPa is well reflected at various directions. It should be noted that based on the model calibrated using experimental results at 0°, 15°, 45° and 90°, satisfying prediction results for the creep deformation at 30° and 70° is also obtained, further demonstrating the model's applicability.

3.1.3. T8 temper 3rd generation Al-Li alloy (0.6 to 0.9 wt.% Li) undergone pre-deformation

This section is for the same alloy in Section 3.1.2 but with pre-deformation treatment. The alloy had undergone 3% ($\varepsilon_{PD} = 0.03$) and 6% PD ($\varepsilon_{PD} = 0.06$) treatment and subsequent creep-ageing at 400 MPa at 143 °C respectively at 0°, 45° and 90° (Wang et al., 2023c). In this case, Eq. (12) is utilised to express the variation of long-range internal stress with pre-deformation following the routine demonstrated in Fig. 4. It is noteworthy that in Eq. (17) which reflects the relationship between the normalised DC length $\overline{l}_\theta$ and the macro PD extents, a θ-dependent parameter μ_θ is used to capture the differences with varying PD & CA directions and is treated as a

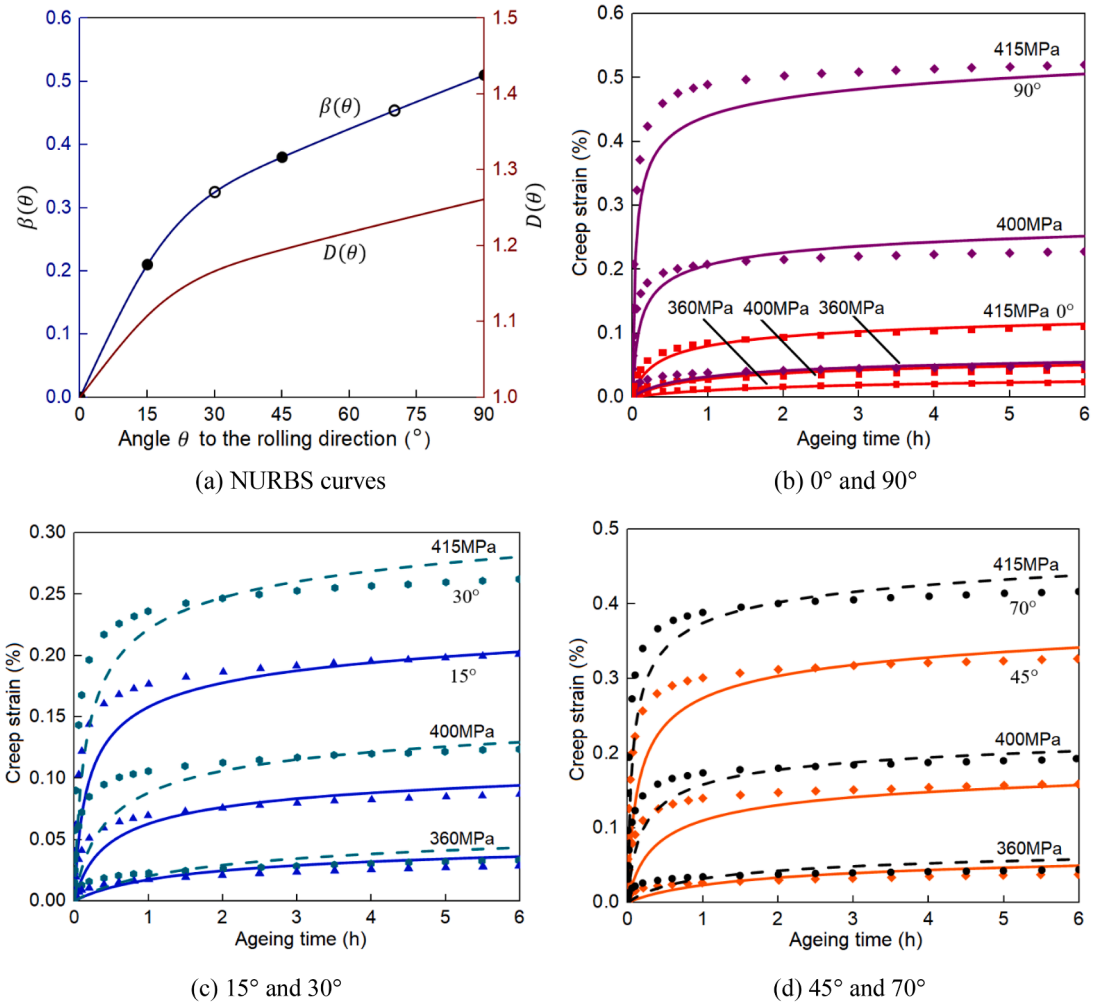

Fig. 6. Comparison of prediction results and experimental data for the 3rd generation Al-Li alloy when creep-aged at different directions and stresses at 143 °C. (a) displays the NURBS curve of $\beta(\theta)$ and $D(\theta)$. (b) to (d) compare the prediction results (lines) with experimental ones (symbols) from (Wang et al., 2023b). The dashed lines of 30° and 70° represent the prediction results obtained from the model calibrated without these data.

Table 4
Employed equations, determined material constants and anisotropic parameters for the pre-deformed 3rd generation Al-Li alloy.

Employed equations for establishing the pre-deformed model								
Equivalent stress: Eq. (24); Macro deformation and DC length: Eq. (17); Stress-creep strain relation: Eq. (20);					Microstructure evolutions: Eq.(1–1) to (1–4); Long range internal stress: Eq. (12) Model calibration: Eqs. (23) to (26);			
Additional material constants and anisotropic parameters determined in this study								
g	m	k_3	k_4	m_5	m_6	$\mu(0^\circ)$	$\mu(45^\circ)$	$\mu(90^\circ)$
696.2	0.3	20.54	15.8	1	2	0	0.53	0.82

function $\mu(\theta)$ using the NURBS curve. Since the alloy is identical to that in Section 3.1.2, the material constants and anisotropic parameters listed in Table 3 are the same. Table 4 lists the equations for the model and the additional constants and parameters used for extending to the scenario of PD & CA.

Fig. 7a demonstrates the established NURBS curve of $\mu(\theta)$ and correspondingly derived evolution curves of $\overline{l_\theta}$ for different directions. The curve of $\mu(\theta)$ is established with fitted values at 0°, 45°, 90°. With the changing $\mu(\theta)$ value, different trends in$\overline{l_\theta}$ evolution are observed with increasing PD at varying directions. The long range internal stress variation $\Delta\tau_l$ is demonstrated in Fig. 7b. When pre-deformed at the rolling direction, $\bar{l}$ increases and $\Delta\tau_l$ decreases with increasing PD. Conversely, $\Delta\tau_l$ increases at 45° and 90° with higher PD. Since $\Delta\tau_l$ provides resistance to creep deformation, higher $\Delta\tau_l$ value would result in lower creep strain. This opposite evolution trend in creep deformation at different direction is adequately captured by the prediction results presented in Fig. 7c to 7e. Furthermore, the prediction results with the available experimental data (Fig. 7f) show a good agreement for precipitation evolution of the materials undergone 6% PD at 0°, 45° and 90°.

3.1.4. T3 temper AA2219

AA2219 is another widely adopted material for fabricating components for aircrafts, which has been extensively studied in CAF research (Ma et al., 2018; Yang et al., 2020). The anisotropic creep behaviour of AA2219-T3 was investigated at 0°, 45° and 90° through uniaxial creep-ageing tests at 120 MPa and 165 °C in (Chen et al., 2020). The used equations, material constants, and anisotropic parameters are listed in Table 5, with further illustration of the fitting process for σ_{th0} presented in Appendix B. The prediction results are demonstrated in Fig. 8.

3.1.5. Largely pre-deformed T4 temper AA2219

The anisotropic creep-ageing behaviour of a largely pre-deformed T4 temper AA2219 was previously investigated (Chen et al., 2022). In the investigation, the PD process involved cold-rolling along the rolling direction resulting a thickness reduction from 11.5 mm to 2 mm with an accumulative equivalent plastic strain around 2.02 ($\varepsilon_{PD} = 2.02$) (Chen et al., 2022). Uniaxial creep-ageing tests were conducted at 140 °C under 150 MPa (at 0°, 15°, 30°, 45°, 60°, 75° and 90° to the rolling direction) and 100 MPa (at 0°, 45° and 90°). Under large pre-deformation, the saturated state of dislocation density has been reached and an initial value of 1 is set for the normalised dislocation density for creep-ageing as described in Section 2.1.

Based on the statistical results of the length ($2a_1$) to width ($2b_1$) ratio of DCs for the largely deformed AA2219-T4, the ratio is set to be 3, i.e. $a_1 = 3b_1$ (Chen et al., 2022). It is worth noting that the exact values of a_1 or b_1 do not affect the value of $\overline{l_\theta}$, as both a_1 and b_1 are eliminated and only their ratio is kept during normalisation. Thus, the variation of long range internal stress induced by DC morphology change with largely pre-deformation can be calculated using Eq. (12). Table 6 demonstrates the used equations, material constants, and anisotropic parameters.

The evolution of the long range internal stress difference $\Delta\tau_l$ with increasing angle θ was determined using Eq. (12) and is demonstrated in Fig. 9a. $\Delta\tau_l$ increases with increasing angle θ, which is induced by the variation of l_θ at different angles in the largely deformed DC. The values of $\beta(\theta)$ for 15°, 30°, 60°, and 75° (the hollow circles in Fig. 9a) are obtained from the same curve determined in Section 3.1.4 for the same alloy. The prediction results for the creep strain curves exhibit satisfying agreements with experimental data (Fig. 9b - 9d). It should be noted that the prediction results of 15°, 30°, 60°, and 75° under 150 MPa presented in Fig. 9c are derived using the predicted values of $\beta(\theta)$ from the NURBS curve which did not use the data for these directions to determine the material constants, demonstrating the prediction accuracy.

3.2. Validation for strength evolution prediction

3.2.1. Strength evolution of pre-deformed 3rd generation Al-Li alloy

As manifested in Eq. (22–2), the material strength evolution during creep-ageing is affected by the evolution of intrinsic strength σ_i, precipitation hardening σ_{ppt}, and dislocation hardening σ_{dis}. In addition, the initial values of σ_i, σ_{ppt}, and σ_{dis} subjected to different pre-treatments can be obtained using an established determination method and equations as (Wang et al., 2022b)

$$\begin{cases} \sigma_{i0} = \sigma_{y1} \\ \sigma_{dis0} = \sigma_{y2} - \sigma_{y1} \\ \sigma_{ppt0} = \left(\left(\sigma_y - \sigma_{i0}\right)^{n_y} - {\sigma_{dis0}}^{n_y}\right)^{1/n_y} \end{cases} \tag{28}$$

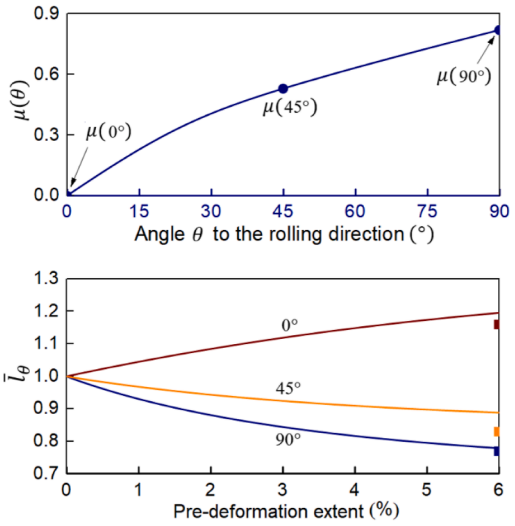

(a) NURBS curve of $\mu(\theta)$ and evolution of $\overline{l_\theta}$

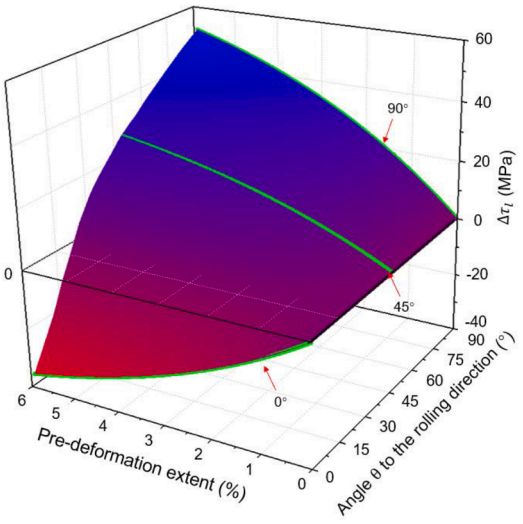

(b) Evolution of $\Delta\tau_l$

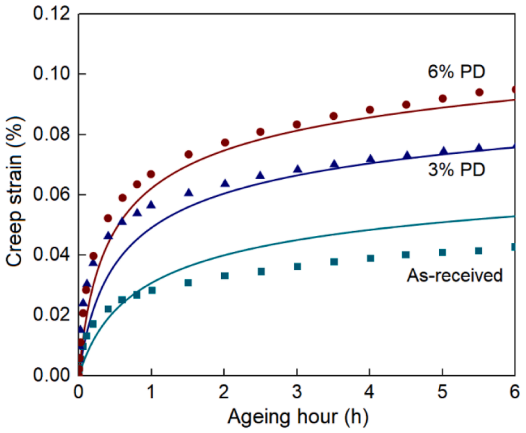

(c) Creep deformation at 0°

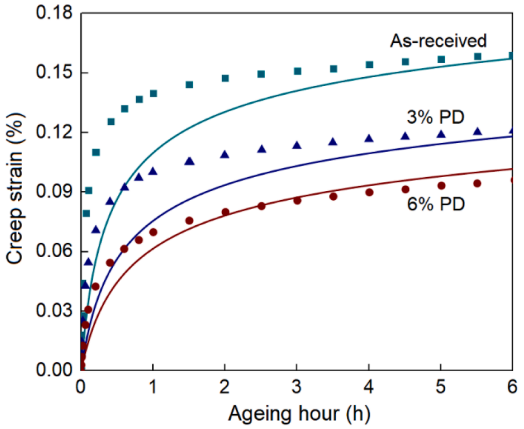

(d) Creep deformation at 45°

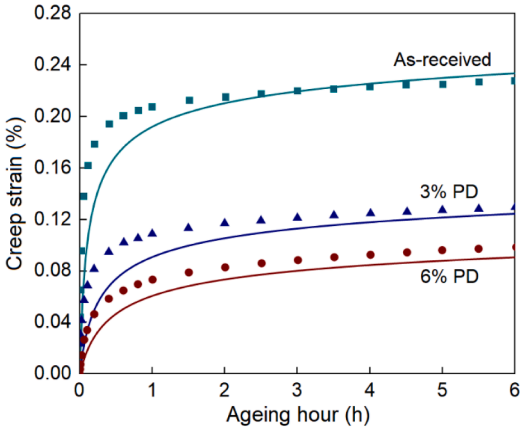

(e) Creep deformation at 90°

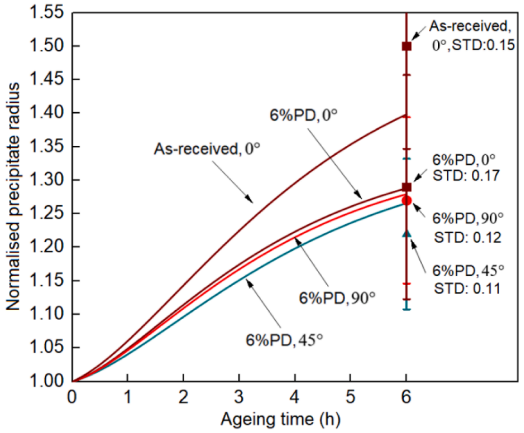

(f) Precipitation evolution

(caption on next page)

Fig. 7. Comparison of model prediction results (curves) and experimental results (symbols) for the 3rd generation Al-Li alloy under PD & CA conditions. The symbols in (a) represent the statistical results of experimental observation, which is further illustrated in Appendix C. (b) exhibits the evolution of long range internal stress change with respect to the variation of pre-deformation extents and directions. The symbols in (c) to (f) denote the creep deformation experimental results obtained under 400 MPa at 143 °C from (Wang et al., 2023c), while the lines depict the prediction results. In (c) to (f), 'As-received' refers to the T8 temper state, and 'PD' stands for the pre-deformation treatment. The pre-deformation extents and directions are also marked in (f). 'STD' in (f) represents the standard deviation of the experimental data from (Wang et al., 2023c).

Table 5
Employed equations, determined material constants and anisotropic parameters for AA2219-T3.

Employed equations							
Equivalent stress: Eq. (24); Stress-creep strain relation: Eq. (7);				Microstructure evolutions: Eqs.(1–1) to (1 - 4); Model calibration: Eqs. (23) to (26);			
Material properties from (Chen et al., 2020)							
σ_0 (MPa)		σ_{45} (MPa)		σ_{90} (MPa)			
239		222		229			
Material constants and anisotropic parameters determined in this study							
A_1 (h^{-1})	A_3 (h^{-1})	B_1 (MPa^{-1})	C_1	C_p	C_r (h^{-1})	F_2	N_2
20	4.3E-4	4E-2	400	1.5E-3	6E-2	0.65	2.4
k_1	k_2	m_1	m_2	m_3	m_4	m_5	m_6
0.5	5.2E-2	0.522	0.95	1.36	1.5	1	1
n_2	n_3	Q_1	$\beta(0°)$	$\beta(45°)$	$\beta(90°)$	γ_0	σ_{th0} (MPa)
2.5	1.5	2.8	0	−0.06	−0.16	8	43

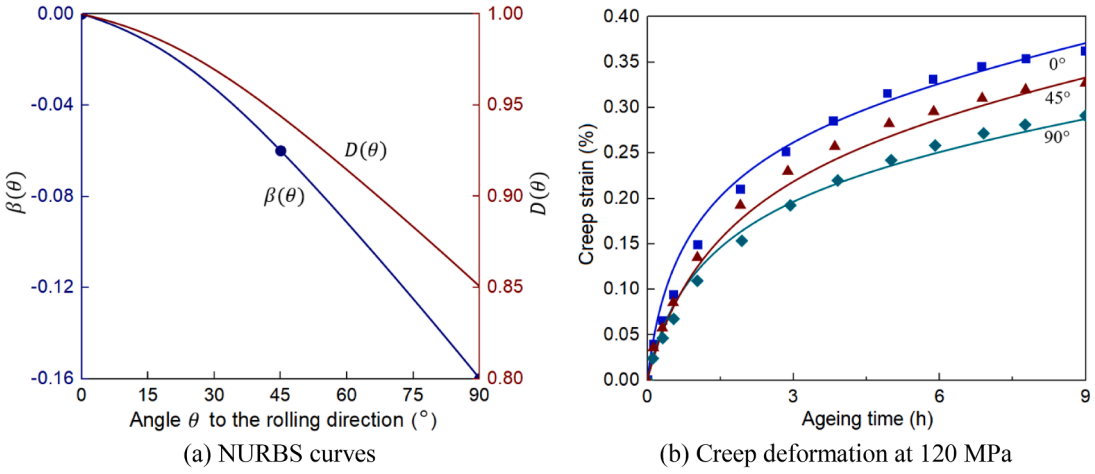

Fig. 8. Fitting and prediction results of AA2219-T3 model. (a) presents the NURBS curve of $\beta(\theta)$ established using the experimental data (symbols) and correspondingly determined curve of $D(\theta)$. (b) demonstrates the creep deformation prediction results under 120 MPa and 165 °C at directions of 0°, 45° and 90°.

Table 6
Material constants for the largely pre-deformed AA2219-T4.

Employed equations for establishing the largely pre-deformed AA2219-T4 model							
Equivalent stress: Eq. (24); Long range internal stress: Eq. (12) Model calibration: Eqs. (23) to (26);				Microstructure evolutions: Eq.(1–1) to (1 - 4); Stress-creep strain relation: Eq. (7);			
Material constants determined in this study							
A_1 (h^{-1})	A_3 (h^{-1})	B_1 (MPa^{-1})	C_1	C_p	C_r (h^{-1})	F_2	N_2
0.1	8.9E-4	3.45E-2	900	0.8	6E-2	0.58	2.4
g	k_1	k_2	m	m_1	m_2	m_3	m_4
1.96E-2	6E-2	0.15	6.26	0.85	0.95	0.55	1.5
m_5	m_6	n_2	n_3	Q_1	γ_0	σ_{th0} (MPa)	
0.33	0.636	3.8	1.5	2.8	8	34	

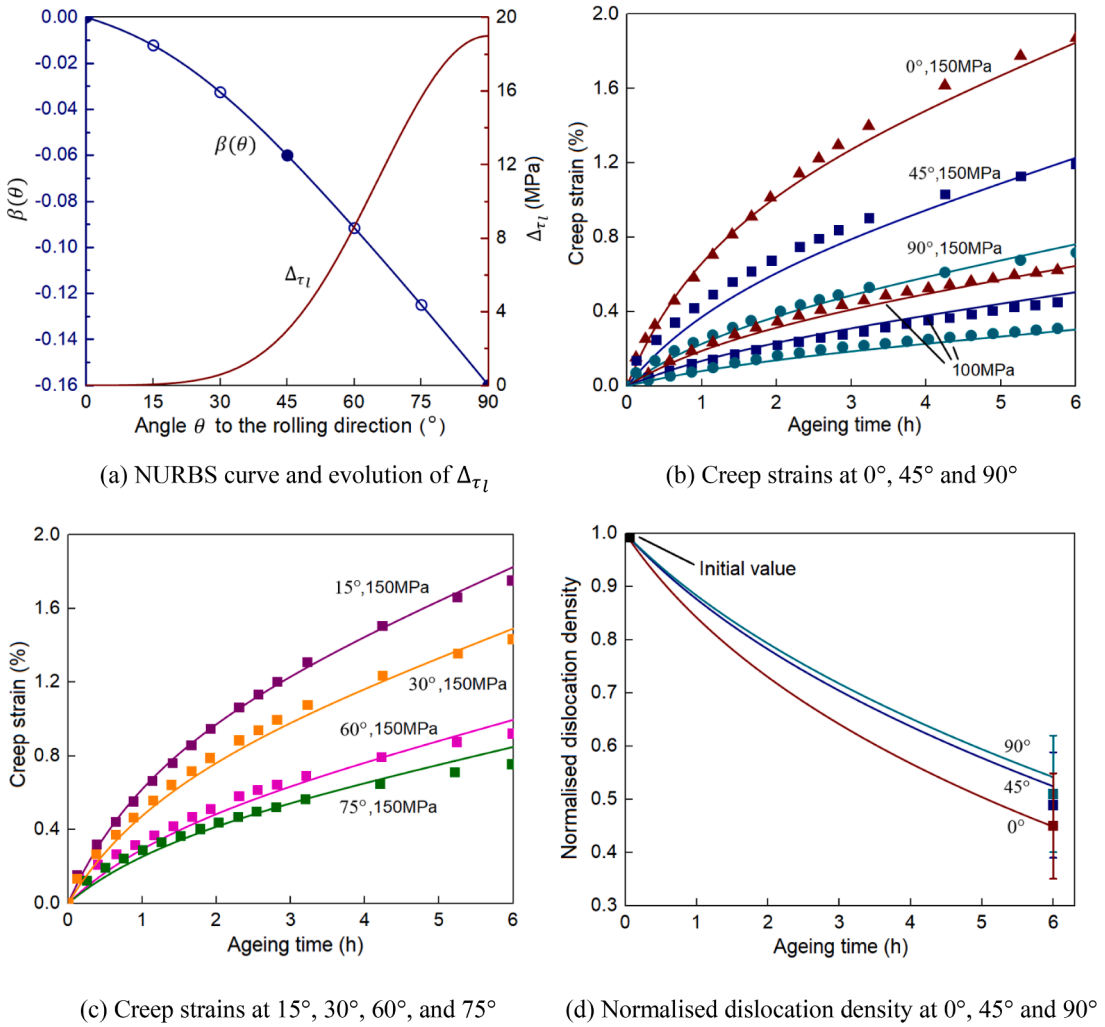

(a) NURBS curve and evolution of $\Delta_{\tau l}$

(b) Creep strains at 0°, 45° and 90°

(c) Creep strains at 15°, 30°, 60°, and 75°

(d) Normalised dislocation density at 0°, 45° and 90°

Fig. 9. Comparison of prediction with experimental results for the largely pre-deformed AA2219-T4. (a) presents the NURBS curves of $\beta(\theta)$ and long-range internal stress difference $\Delta_{\tau l}$ with increasing angle θ. The hollow symbols at 15°, 30°, 60°, and 75° are values obtained from the established NURBS curve for prediction verification. (b) and (c) illustrate the prediction results of creep deformation in comparison with experimental data (solid symbols) from (Chen et al., 2022) under 150 MPa at 140 °C in directions of 0°, 45° and 90° (in (b)), and 15°, 30°, 60°, and 75° (in (c)). (d) demonstrates the prediction and experimental results of the normalised dislocation density at 0°, 45° and 90° under 100 MPa at 140 °C. The experimental results are from (Chen et al., 2022).

Table 7
Strength model for pre-deformed 3rd generation Al-Li alloy.

Employed equations						
Dislocation hardening σ_{dis0}: Eq. (3–1); Intrinsic material strength σ_i: Eq.(22–1);				Precipitation hardening σ_{ppt}: Eq. (3–2); Material hardening: Eq. (22–2);		
Material constants determined in previous study (Wang et al., 2023c, 2022b)						
A_2 (MPa)	c_1'	c_2'	m_{na}	m_{nb}	n_d	n_y
14	225	365	0.83	0.03	4.2	1.16
σ_{i0} (MPa)	σ_{dis0} (MPa)	σ_{ppt0} (MPa)	σ_{dis0}, 3%PD (MPa)	σ_{dis0}, 6%PD (MPa)		
299	56	140.2	74	90		
Additional material constants determined in this study						
α_1	$\alpha(0^\circ)$	$\alpha(45^\circ)$	$\alpha(90^\circ)$			
12	0	0.08	0.11			

where σ_{i0} represents the initial intrinsic strength equivalent to the yield strength σ_{y1} after SHT and quenching when the alloy has super saturated solid solution. σ_{y2} denotes the yield strength after tensile PD, with the initial value of dislocation hardening σ_{dis0} equals to the difference between σ_{y2} and σ_{y1}. The initial precipitation hardening σ_{ppt0} is derived from the strength contribution relationship in Eq. (28). Table 7 lists the equation numbers for establishing the strength model and the anisotropic parameters and material constants used for strength evolution prediction.

Fig. 10 presents the prediction results for the anisotropic strength evolution with different PD extents ranging from 0% to 6% at 0°, 45°, and 90° directions. As shown in Fig. 10a, the NURBS curve of $\alpha(\theta)$ is established using the determined values at 0°, 45°, and 90° to capture strength anisotropy at the beginning of creep-ageing. Correspondingly, the curves of $\alpha_d(0\text{h},\theta)$ at the beginning and $\alpha_d(6\text{h},\theta)$ at 6 h of creep-ageing calculated using Eq. (22–1) are also displayed in Fig. 10a, showing the diminishing effect of the intrinsic material strength anisotropy with proceeding of creep-ageing. Fig. 10b to 10d exhibit the predicted strength evolutions as well as the specific strength contributions of σ_i, σ_{ppt}, and σ_{dis} of 0% PD at 0°, 45°, and 90°. A good agreement is achieved between the prediction and experimental results in all directions and PD extents, with a maximum material yield strength prediction divergence of 11 MPa (2.1%) for the 6% pre-deformed and creep-aged at 6 h along the rolling direction (0°).

3.2.2. *Strength evolution of AA2219-T3*

In the T3 temper state, the initial contribution of precipitation hardening σ_{ppt0} can be considered negligible, i.e. $\sigma_{ppt0} = 0$, as the precipitation process is in its very early stage. The value of σ_{dis0} is obtained by calculating the difference between the flow stress of the SHTed AA2219 at the strain of 0% and 3% with a value of 69 MPa (Yang, 2013). The equation numbers and the anisotropic parameters

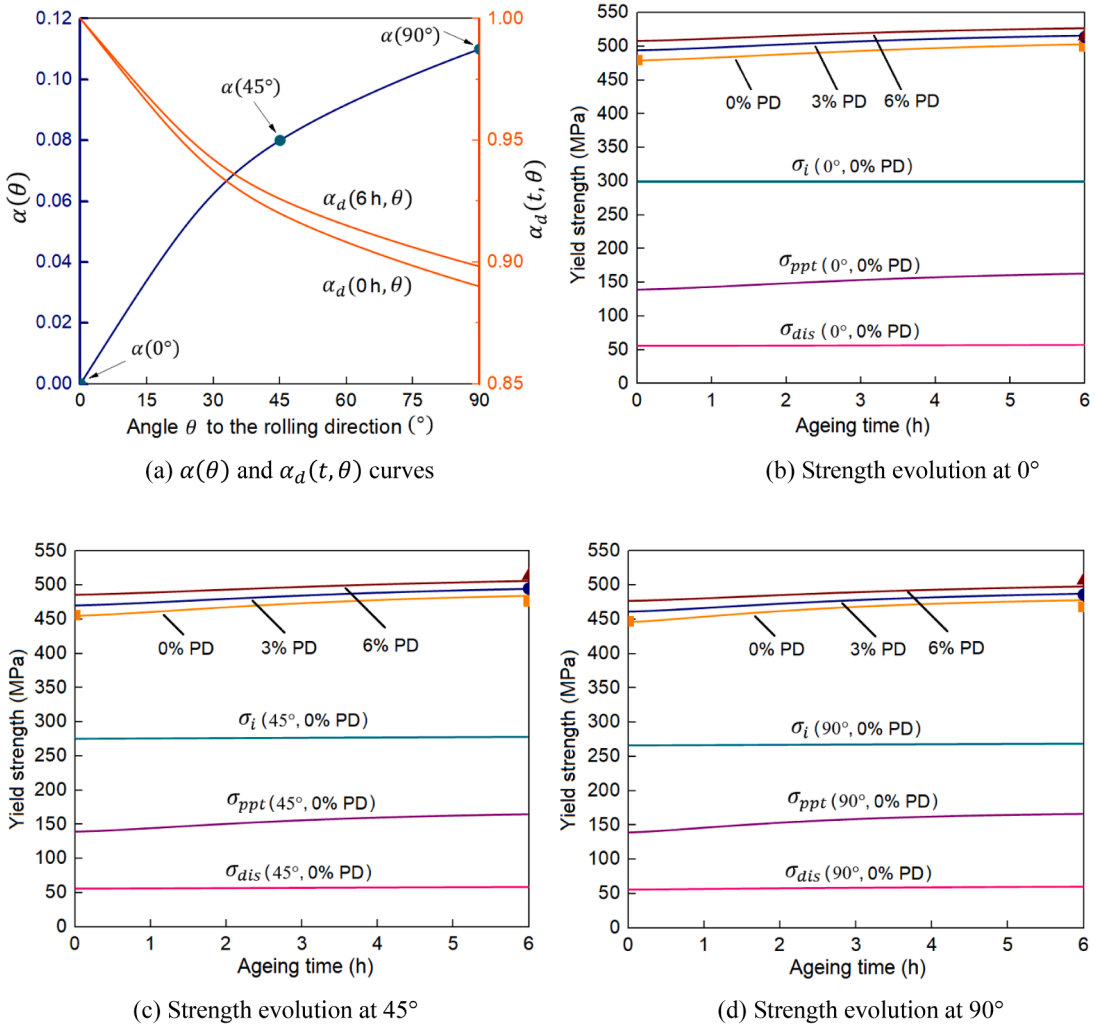

(a) $\alpha(\theta)$ and $\alpha_d(t,\theta)$ curves

(b) Strength evolution at 0°

(c) Strength evolution at 45°

(d) Strength evolution at 90°

Fig. 10. The strength evolution prediction results. (a) presents the NURBS curve of $\boldsymbol{\alpha}(\boldsymbol{\theta})$ and the corresponding $\boldsymbol{\alpha_d}(\boldsymbol{\theta})$ at 0 and 6 h in creep-ageing. The solid symbols in (a) are the values of $\boldsymbol{\alpha}(\boldsymbol{\theta})$ for establishing the curve. (b) to (d) demonstrate respectively the strength evolution prediction results at 0°, 45°, and 90° for 0%, 3%, 6% pre-deformation (PD) extents. The solid symbols in (b) to (d) denote experimental data from (Wang et al., 2023c).

Table 8
Strength model for AA2219-T3.

Employed equations						
Dislocation hardening σ_{dis0}: Eq. (3–1); Intrinsic material strength σ_i: Eq. (22–1);				Precipitation hardening σ_{ppt}: Eq. (3–2); Material hardening: Eq. (22–2);		
Material properties determined from previous study (Yang, 2013)						
σ_{i0} (MPa)		σ_{dis0} (MPa)		σ_{ppt0} (MPa)		
265		69		0		
Material constants determined in this study						
A_2 (MPa)	c_1'	c_2'	m_{na}	m_{nb}	n_d	n_y
25	22	62	0.4	0.3	3	1.16
α_1	$\alpha(0^\circ)$	$\alpha(45^\circ)$	$\alpha(90^\circ)$			
5.5	0	0.08	0.13			

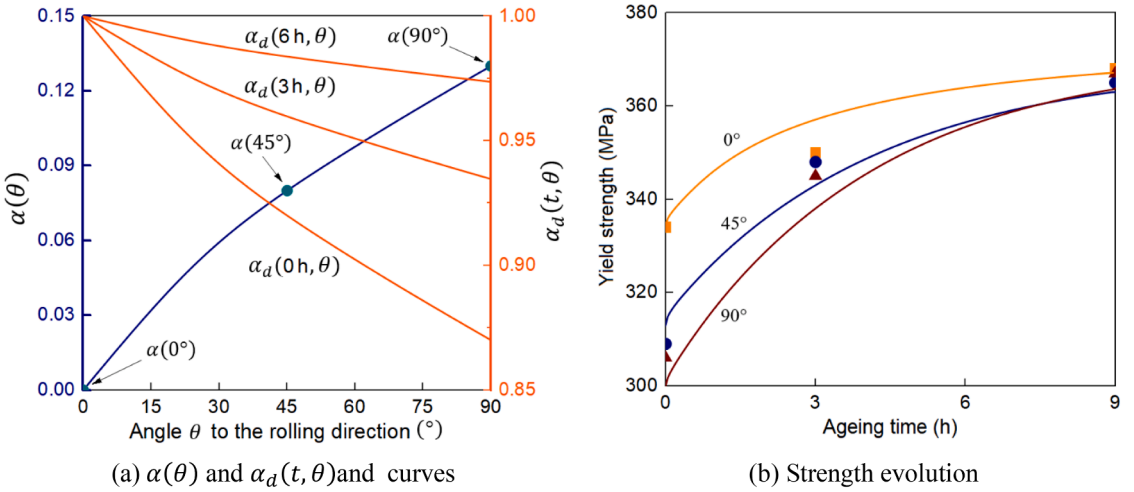

(a) $\alpha(\theta)$ and $\alpha_d(t,\theta)$and curves (b) Strength evolution

Fig. 11. Strength evolution prediction results. (a) exhibits the NURBS curve of $\alpha(\theta)$ and the corresponding curve of $\alpha_d(\theta)$ at 0, 3 and 6 h in creep-ageing. The symbols in (a) represent the $\alpha(\theta)$ values used to establish the curve. (b) shows the strength evolution at 0°, 45°, and 90° with creep-ageing time, with solid symbols representing experimental results from (Yang, 2013).

as well as the material constants used for strength prediction of AA2219-T3 are given in Table 8.

Fig. 11 presents the strength evolution prediction results for AA2219-T3. The NURBS curve of $\alpha(\theta)$ is established in Fig. 11a and the values increase with angle θ. The values of $\alpha_d(\theta)$ demonstrate an opposite trend, all decreasing with increasing angle θ at 0, 3, and 6 h of creep-ageing. On the other hand, $\alpha_d(\theta)$ demonstrates an obvious trend toward unity at all directions with increasing ageing time. As a result, Fig. 11b illustrates the gradual reduction of anisotropy in σ_y and the IPA of strength reduces from 7.9% at 0 h to 0.5% at 9 h.

3.2.3. *Strength evolution of largely pre-deformed AA2219-T4*

For AA2219-T4, the same initial intrinsic strength σ_{i0} of AA2219-T3 is adopted. In addition, the value of initial precipitation hardening σ_{ppt0} in the T4 temper is identical to T3 as 0. The value of σ_{dis0} can be obtained utilising Eq. (28). The calibrated anisotropic parameters and material constants are presented in Table 9.

Fig. 12a shows the NURBS curve of $\alpha(\theta)$. The values of $\alpha(15^\circ)$ and $\alpha(75^\circ)$ are obtained from the predicted curve for verification

Table 9
Strength model for largely pre-deformed AA2219-T4.

Employed equations							
Dislocation hardening σ_{dis0}: Eq. (3–1); Intrinsic strength σ_{dis0}: Eq.(22–1);					Precipitation hardening σ_{ppt}: Eq. (3–2); Material hardening: Eq. (22–2);		
Material constants determined in this study							
A_2 (MPa)	c_1'	c_2'	m_{na}	m_{nb}	n_d	n_y	σ_{dis0} (MPa)
135	8	2	0.2	0.3	0.58	1.16	240
α_1	$\alpha(0^\circ)$	$\alpha(30^\circ)$	$\alpha(45^\circ)$	$\alpha(75^\circ)$	$\alpha(90^\circ)$		
20	0	0.02	0.05	-0.03	-0.045		

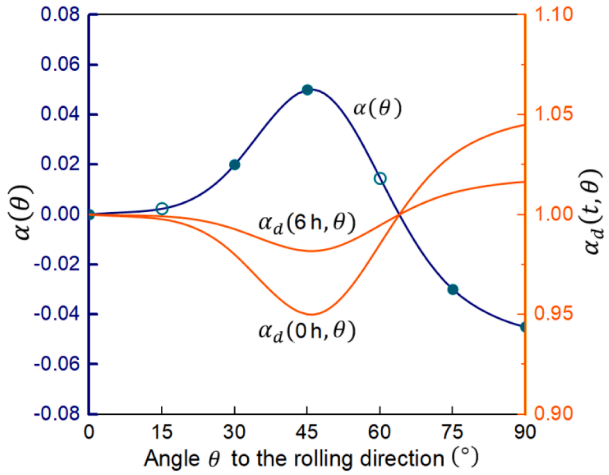

(a) NURBS curve of $\alpha\,(t,\theta)$

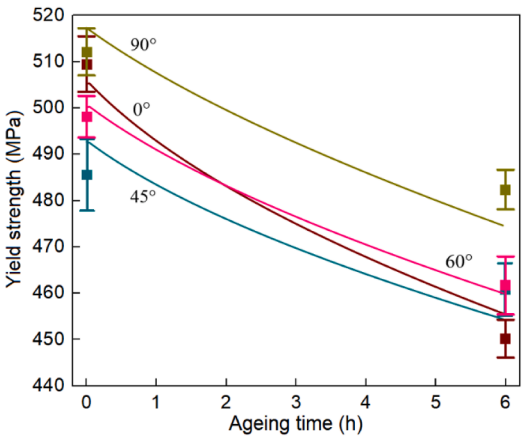

(b) Results from 0°, 45°, 60°, and 90°

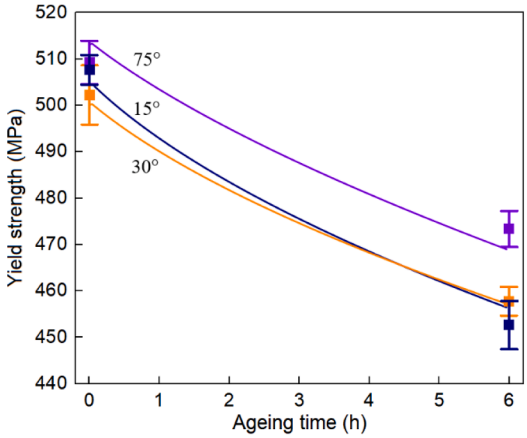

(c) Results from 15°, 30°, 75°

Fig. 12. The NURBS curve of $\boldsymbol{\alpha}(\boldsymbol{\theta})$ and strength evolution prediction results. The solid symbols in (a) are used for establishing the curve, the hollow circles are prediction values obtained from the established curve. (b) and (c) present the strength evolution prediction results at different angles ranging from 0° to 90°. The solid symbols with error bars in (b) and (c) stand for the experimental data from (Chen et al., 2022).

purpose. The curves of $\alpha_d(\theta)$ at 0 and 6 h of creep-ageing are also displayed in Fig. 12a. The latter curve of 6 h has more stable values approaching unity than the former of 0 h. Fig. 12b and c demonstrate the prediction results of the strength evolution at various angles ranging from 0° to 90°. It can be observed the prediction results at different angles including both fitting determined (0°, 30°, 60°, and 90°) and the predicted ones for verification (15° and 75°), manifest an adequate level of accuracy when compared with the experimental results.

In summary, this section demonstrates that satisfying agreements are achieved between the prediction and experimental results regarding anisotropic creep deformation and strength evolution in creep-ageing. This consistency indicates that the established model is able to produce reliable predictions by following the proposed model construction routine. It should be noted that the anisotropic creep-ageing behaviour of various 2xxx series Al alloys can vary significantly between different alloys, due to their different chemical compositions, precipitates and temper states. More material constants are needed to extend the previously proposed rolling-direction based isotropic material model to an anisotropic one, aiming at describing the different anisotropic creep deformation behaviour of various 2xxx series Al alloys with a generalised form. As a result, it is challenging to incorporate material constants with the same value into this framework to establish material models that can accurately capture the diverse anisotropic creep-ageing behaviours of various 2xxx Al alloys. Among the 26 basic material constants employed in all cases, 16 of them are calibrated within a narrow value range or have the same value in this study, aiming to improve the convenience and applicability of this framework. This is further summarised in Appendix A.

3.3. Application to four-point bending CAF

Although there have been many studies investigating the anisotropic creep-ageing behaviour, few have explored the effect of anisotropy on practical creep age forming beyond the uniaxial tests, apart from the authors' investigation on the 3rd generation Al-Li alloy. Hence, the constitutive model for T8 temper 3rd generation Al-Li alloy, established in Section 3.1.2, was implemented in numerical simulation to validate its applicability and prediction accuracy. Fig. 13 shows the schematic of a four-point bending assembly, boundary conditions, and dimensions of the finite element (FE) model. The FE model had a dimension of 220 × 18 × 2 (mm) with its X-Z symmetry plane as shown in the figure. The loading displacement was 20.2 mm with subsequent CAF for 5 h, aiming at fabricating sheets with a curvature of 2000 mm^{-1}. In the FE model, the loading and supporting heads were composed of discrete rigid elements with dimensions of 1.5 × 1.5 (mm). C3D8R elements with dimension of 1 × 1 × 0.33 (mm) were used for the specimen. The surface contacts between the loading/supporting heads and the specimen were modelled by tangential behaviour with a friction coefficient of 0.25.

The constitutive model was implemented in the simulation following the CAF procedure including loading, creep-ageing, and unloading stages. In the loading stage, a downward displacement of 20.2 mm was applied on the loading heads. During this process, the yielding check and plastic strain calculation was conducted by employing a map returning and bisection method. The details of yielding check and plastic strain determination have been introduced in (Wang et al., 2023b). In the subsequent creep-ageing stage, the equivalent creep strain increment ($d\bar{\varepsilon}^{cr}$) in each integration step with a time length of Δt was computed using Eq. (20) as $d\bar{\varepsilon}^{cr} = \dot{\bar{\varepsilon}}^{cr}\Delta t$. The creep strain increment components ($d\varepsilon_{ij}^{cr}$) were obtained using Eq. (25) and the stress state at the end of k^{th} integration step ($^{k}\boldsymbol{\sigma}'$) was determined using Eq. (27). In the unloading stage, the stress state was updated following the equation as $^{k}\boldsymbol{\sigma}' = {}^{k-1}\boldsymbol{\sigma}' + \boldsymbol{C_e}\Delta\boldsymbol{\varepsilon_e}$, where $\boldsymbol{C_e}$ denote the elastic stiffness tensor and $\Delta\boldsymbol{\varepsilon_e}$ represents the elastic strain increment within the integration step.

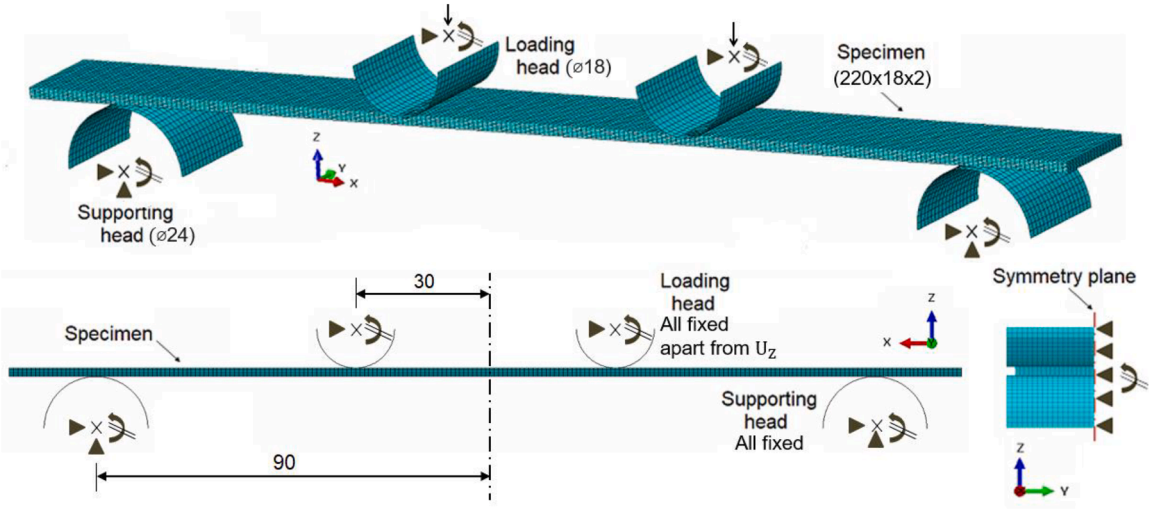

Fig. 13. Schematic of the FE model (dimension mm).

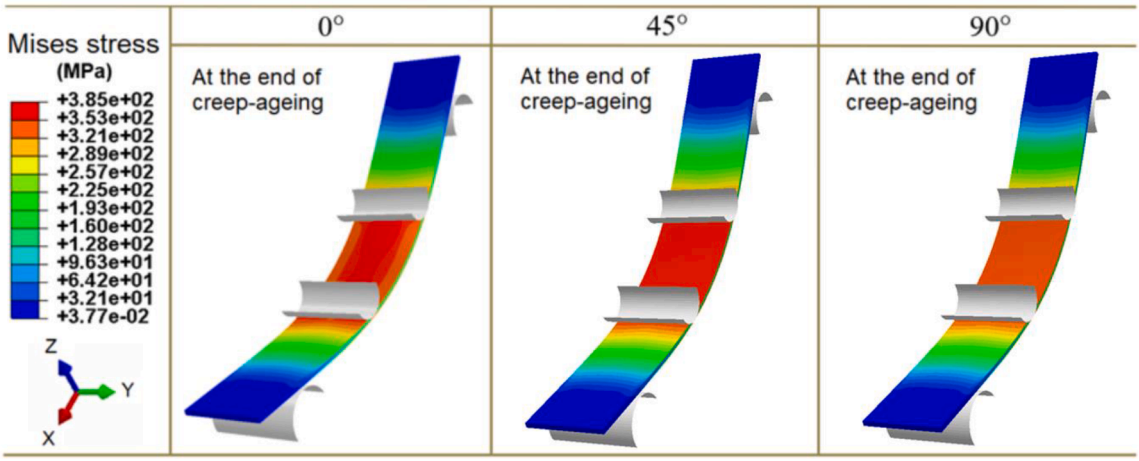

(a) Simulated stress distributions at the end of creep-ageing at 0°, 45°, and 90°

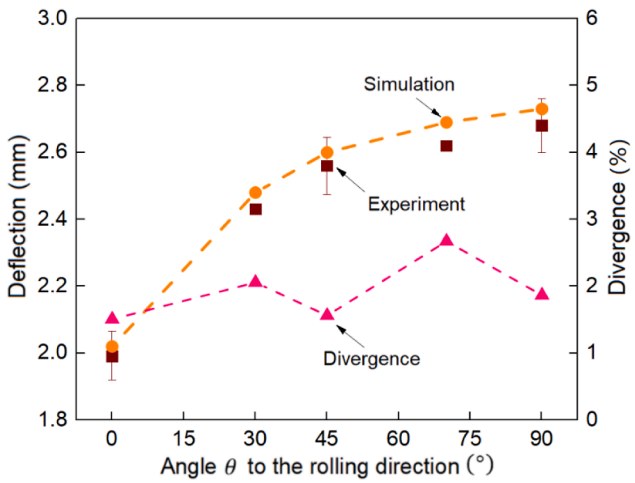

(b) Simulated and experimental deflections and divergence

Fig. 14. FE simulation and experimental results for creep age forming with materials at different directions. (a) shows the simulation results of stress states at the end of creep-ageing. (b) illustrates the final deflection results after springback from experiments and simulation, as well as their divergences. The squares in (b) represents experimental data from (Wang et al., 2023b).

Fig. 14a displays the FE simulated von Mises stress distributions at the end of creep-ageing for 0°, 45°, and 90° directions. Different stress results are obtained at different directions due to anisotropic behaviour, which leads to various final deflections after springback. Fig. 14b shows the final deflection results from the experiments and FE simulations as well as the deflection divergence in percentage at different directions. The percentage of deflection divergence is calculated by the ratio of the difference between the simulation and experimental results to the latter. It can be observed that the prediction results demonstrate good agreements with the experimental data. Overall, the simulated deflections are slightly larger than the experimental averages within the range of 0.03 to 0.07 mm, well within the experimental spread. The maximum divergence of 0.07 mm occurred at 70°, with corresponding 2.7% divergence to the experimental data. This illustrates the feasibility and prediction accuracy by implementing the anisotropic model in numerical simulation, indicating that the established model can be used in process simulation for springback prediction and compensation for die surface design.

The reliability of the framework-established models in generating accurate prediction results has thus been verified in two ways. Firstly, the prediction accuracy of the model is verified by using data points at specific angles which are not used to determine the material constants (see Fig. 9c). Secondly, the model is implemented in the FE simulation for verifying its prediction accuracy in practical creep age forming tests (see Fig. 14). The prediction results in both ways demonstrate good agreements with the experimental data, confirming the model's reliability despite more necessary material constants.

4. Conclusions

This study provides a generalised framework for developing anisotropic creep-ageing material models by employing NURBS function to consecutively predict the creep deformation behaviour at varying angles between the loading and rolling directions, as well as routines for model calibration with experimental results and implementation in numerical simulation. The framework demonstrates its feasibility to construct models that capture the anisotropic behaviours in both constitutive modelling and numerical simulation through examples of various 2xxx Al alloys. The major findings can be summarised as follows:

(1) By incorporating NURBS-expressed anisotropic coefficients, this framework becomes generalisable for constructing material models able to capture the intricate anisotropic behaviours related to both creep deformation and strength, while also maintaining the ability to reflect microstructural evolutions. The prediction accuracy is validated with experimental data of various alloys with or without pre-deformation, including 2xxx series aluminium alloys AA2195 and AA2219, and 3rd generation Al-Li alloy with 0.6 to 0.9 wt.% Li.
(2) The established relationship between macro deformation and changes in micro dislocation cell morphology, along with its impact on internal stress variation, can adequately capture the anisotropy evolution of creep deformation and material strength for alloys pre-deformed with varying extents at specific directions from 0° to 90°.
(3) This framework includes the calibration and implementation methods to ensure the consistency between material modelling and numerical simulation by employing a transformation routine between the predicted equivalent and measured strains. The simulation results demonstrate satisfactory agreement with four-point bending CAF test results at different directions, with a maximum deflection divergence of 2.7% at 70°.

CRediT authorship contribution statement

Xi Wang: Writing – original draft, Visualization, Investigation. **Zhusheng Shi:** Writing – review & editing, Supervision, Conceptualization. **Jianguo Lin:** Writing – review & editing.

Declaration of competing interest

The authors declare that they have no known competing financial interests or personal relationships that could have appeared to influence the work reported in this paper.

Data availability

Data will be made available on request.

Appendix A. Material constants determination and summary

A widely adopted combination of forward Euler method and least square method was employed in this study for material constants determination. The forward Euler method was adopted to solve the non-linear ordinary differential equations:

$$s_{n+1} = s_n + \dot{s}_n \Delta t \tag{A1}$$

where s_{n+1} and s_n are values of internal variable s at time step $n+1$ and n respectively; $\dot{s}_n$ is the evolution rate at time step n; Δt is the time increment.

The least square method was adopted to determine the material constants for the model to be best fitted with experimental data. The objective function is written as

$$f(x) = \sum_{i=1}^{L2} \sum_{j=1}^{L3} \sum_{k=1}^{L4} \left(y_{ijk}^{m} - y_{ijk}^{e} \right) \tag{A2}$$

where $x = (x_1, x_2, x_3, \ldots, x_{L1})$ is the material parameters with a total number of $L1$ to be determined in the model. $L2$ is the number of series classified by the loading angles used for fitting. $L3$ is the number of applied stresses in each loading angle. $L4$ is the number of data points at the specific loading angle and stress. y_{ijk}^{m} and y_{ijk}^{e} stand for the model-determined value and experimental data value of i th loading direction, j-th stress series, and k-th data point respectively.

It can be observed from Section 3 that for different 2xxx series aluminium alloys, the anisotropic creep-ageing behaviour can vary significantly. However, the fitting results of the material constants for various 2xxx Al alloys in this study demonstrate that there exist constants which can be determined within a narrow value range, i.e. the upper and lower limit values of a constant determined for various 2xxx Al alloys in this study are of the same magnitude or their ratio is less than 10. The material constants with the characteristic of narrow value range in this study are summarised in Table A1, providing a basis for future application of the model to other 2xxx aluminium alloys.

Table A1
Material constants with narrow value range for anisotropic creep deformation and strengthening in creep-ageing.

Material constants for creep deformation					
A_1 (h^{-1})	B_1 (MPa^{-1})	C_r (h^{-1})	F_1 or F_2	m_1	m_2
0.1 to 26	2.5E-2 to 4E-2	6E-2 to 8E-2	0.58 to 3.8	0.482 to 0.85	0.75 to 0.95
m_3	m_4	N_1 or N_2	Q or Q_1	γ_0	
1.05 to 1.36	1.5	2.45 to 3	0.68 to 2.8	0.96 to 8	
Material constants for strengthening					
c_1'	c_2'	m_{na}	m_{nb}	n_y	
8 to 225	2 to 365	0.2 to 0.83	3E-2 to 3E-1	1.16	

Appendix B. Determination of the initial threshold stress

This study adopts a previously proposed linear extrapolation method for determining the initial threshold stress σ_{th0} (Wang et al., 2022b). The steady state creep rate can be expressed using the equation as

$$\dot{\varepsilon} = A^{*}(\sigma - \sigma_{th0})^{n} \exp\left(\frac{-Q_a}{RT}\right) \tag{B1}$$

where A^{*} is material constants. n is the stress exponent. Q_a, R, and T are respectively the activation energy, gas constant, and the absolute temperature. The logarithm form of Eq. (A1) can be written as

$$\ln(\dot{\varepsilon}) = n \ln(\sigma - \sigma_{th0}) + \ln(A^{*} \exp(-Q_a/RT)) \tag{B2}$$

By employing Eqs. (B1) and (B2), σ_{th0} can be determined following the fitting procedure of the linear extrapolation method. The results are presented in Fig. B. Fig. B1a and B1b demonstrates the fitting results for the AA2195-T3 with the stress exponent $n = 1.41$ and initial threshold stress $\sigma_{th0} = 11$ MPa. Fig. B1c and B1d shows the fitting results of AA2219-T3 with $n = 2.07$ and $\sigma_{th0} = 43$ MPa. Fig. B1e and B1f presents the fitting results of AA2219-T4 with $n = 1.85$ and $\sigma_{th0} = 34$ MPa.

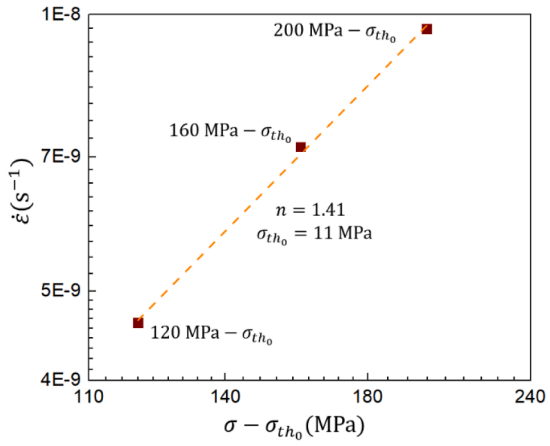

(a) $\dot{\varepsilon}$ vs $(\sigma - \sigma_{th_0})$ for AA2195-T3

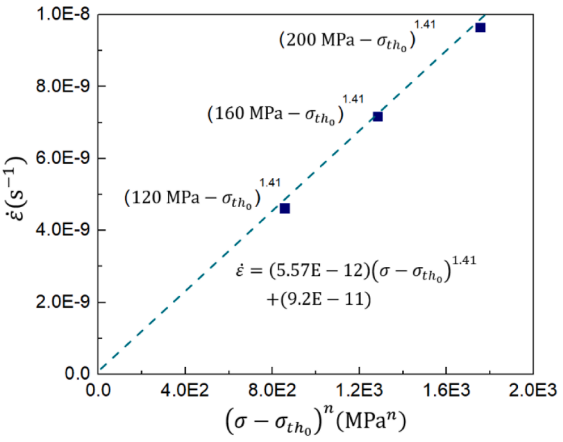

(b) $\dot{\varepsilon}$ vs $(\sigma - \sigma_{th_0})^n$ for AA2195-T3

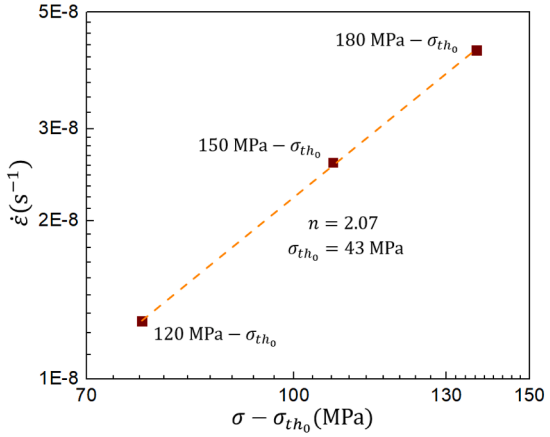

(c) $\dot{\varepsilon}$ vs $(\sigma - \sigma_{th_0})$ for AA2219-T3

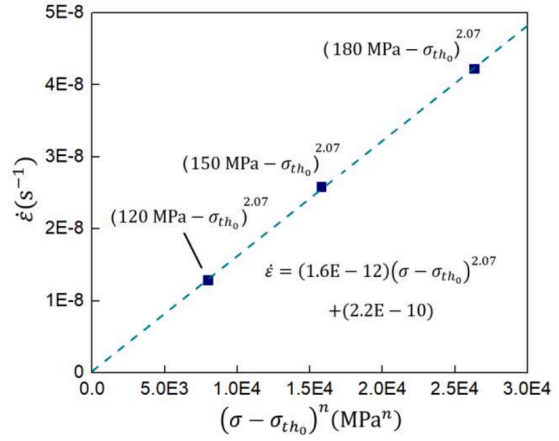

(d) $\dot{\varepsilon}$ vs $(\sigma - \sigma_{th_0})^n$ for AA2219-T3

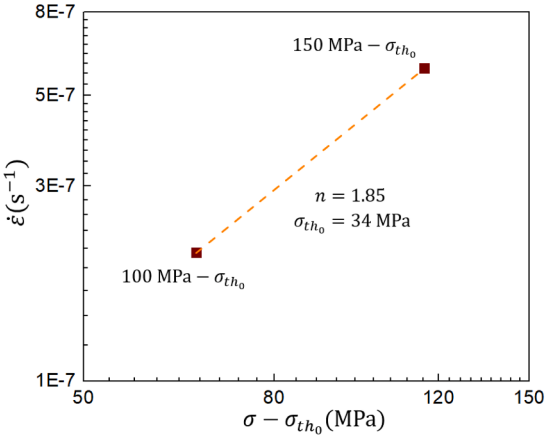

(e) $\dot{\varepsilon}$ vs $(\sigma - \sigma_{th_0})$ for AA2219-T4

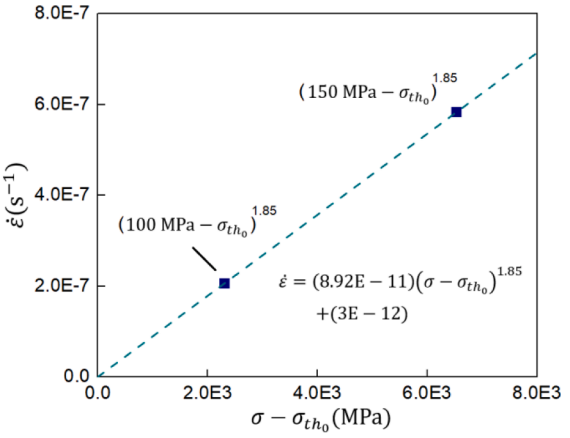

(f) $\dot{\varepsilon}$ vs $(\sigma - \sigma_{th_0})^n$ for AA2219-T4

Fig. B1. Fitting results of the initial threshold stress σ_{th0} for various alloys. (a), (c), and (e) demonstrate the logarithm plot of $\dot{\varepsilon}$ with $(\sigma - \sigma_{th_0})$ to obtain the value of exponential index *n*. (b), (d), and (f) display the plot of $\dot{\varepsilon}$ with $(\sigma - \sigma_{th_0})^n$ to determine whether the criteria are met using the trial values of σ_{th_0} according to the linear extrapolation method.

Appendix C. Study of DC length evolution with PD & CA at 0°, 45°, and 90°

To quantitively investigate the DC length change with PD in the creep-ageing of the 3rd generation Al-Li alloy (0.6 to 0.9 wt.% Li), transmission electron microscopy (TEM) observations were respectively conducted on the as-received material and with treatments of tensile PD to 6% and creep-aged under 400 MPa at 143 °C for 6 h at 0°, 45°, and 90°. TEM investigations were conducted using electropolished 3 mm diameter round foil (thickness less than 80 μm) samples taken from centre area of the specimen and marked with the rolling direction as displayed in Fig. B1a. The measurements of DC length at different directions are exhibited in Fig. C1b to C1e and the results are demonstrated in Fig. C1f and 1g. The data in Fig. C1f are the statistical averages and spreads from 20 DCs for each condition.

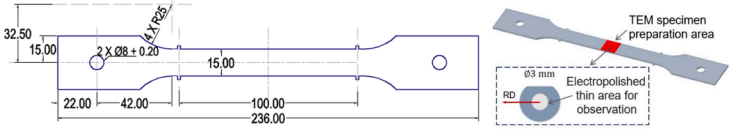

(a) Schematic and dimensions of the specimen

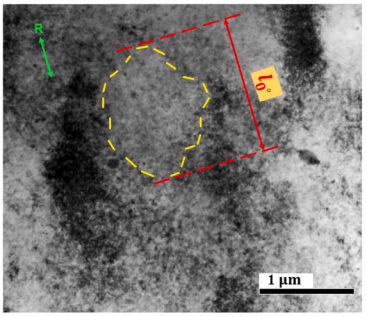

(b) As-received

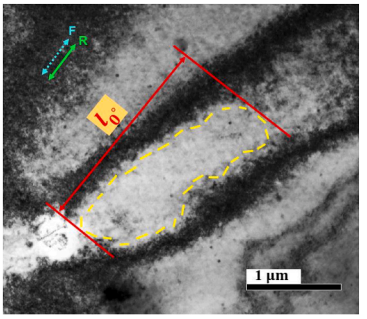

(c) 6% PD & CA at 0°

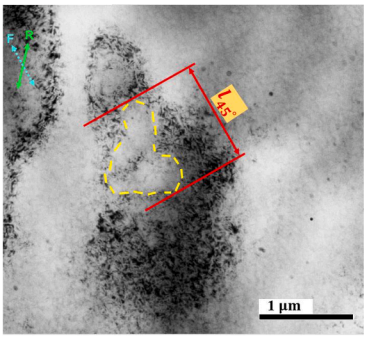

(d) 6% PD & CA at 45°

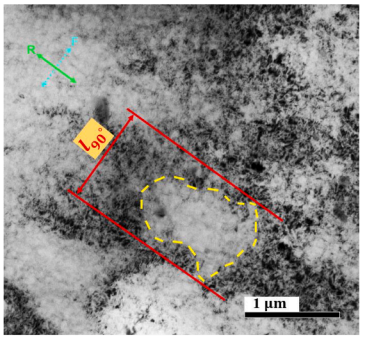

(e) 6% PD & CA at 90°

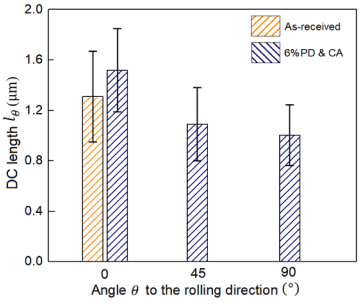

(f) l_θ of as-received and with 6% PD & CA

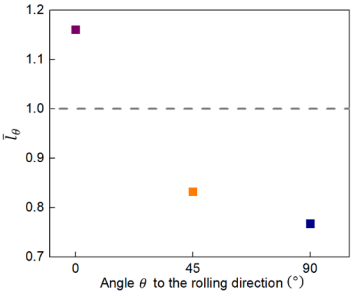

(g) $\bar{l}_\theta$ with 6% PD & CA at 0°, 45°, and 90°

Fig. C1. TEM images of DCs at different conditions and statistical results of the DC length. (a) to (d) demonstrate the TEM images of DC at various conditions including the as-received state and PD & CA at 0°, 45°, and 90°. In (a) to (d), the rolling direction and pre-deformation (loading) direction are denoted with 'R' and 'F'. The variable l_θ indicates the DC length measured at angle θ to the rolling direction. (f) provides the statistical results l_θ of the as-received and after 6% PD & CA, with 20 DCs measured for each state and direction. (g) is the result of the normalised DC length $\bar{l}_\theta$ determined from the statistical average in (f).

References

Aretz, H., 2007. Numerical analysis of diffuse and localized necking in orthotropic sheet metals. Int. J. Plast. 23, 798–840.
Azarniya, A., Taheri, A., Taheri, K., 2019. Recent developments in advanced aircraft aluminium alloys. J. Alloys. Compd. 781, 945–983.
Bian, T., Li, H., Yang, J., Lei, C., Wu, C., Zhang, L., Chen, G., 2020. Through-thickness heterogeneity and in-plane anisotropy in creep aging of 7050 Al alloy. Mater. Des. 196, 109190.
Bodily, B., Heinimann, M., Bray, G., Colvin, E., 2012. Advanced aluminum and aluminum-lithium solutions for derivative and next generation aerospace structures. SAE Tech. Paper, 2012-01-1874.
Cardoso, R., Adetoro, O., 2017. A generalisation of the Hill's quadratic yield function for planar plastic anisotropy to consider loading direction. Int. J. Mech. Sci. 128-129, 253–268.
Chen, K., Liu, C., Ma, P., Yang, J., Zhan, L., Huang, M., Hu, J., 2021a. Enhancing creep formability and comprehensive property in Al–Mg–Si alloy by combinatorial pre-ageing and large pre-deformation. Mater. Sci. Eng.: A 826, 141967.
Chen, L., Liu, C., Ma, P., Yang, J., Zhan, L., Huang, M., 2022. Strong in-plane anisotropy of creep ageing behavior in largely pre-deformed Al-Cu alloy: experiments and constitutive modeling. Int. J. Plast. 152, 103245.
Chen, X., Zhan, L., Xu, Y., Ma, Z., Zheng, Q., 2020. Anisotropy in creep ageing behavior of textured Al-Cu alloy under different stress states. Mater. Charact. 168, 110539.
Chen, X., Zhao, G., Xu, X., Wang, Y., 2021b. Effects of heat treatment on the microstructure, texture and mechanical property anisotropy of extruded 2196 Al-Cu-Li alloy. J. Alloys. Compd. 862, 158102.
Clausmeyer, T., Gerstein, G., Bargmann, S., Svendsen, B., van den Boogaard, A.H., Zillmann, B., 2013. Experimental characterization of microstructure development during loading path changes in bcc sheet steels. J. Mater. Sci. 48, 674–689.
Dannoshita, H., Hasegawa, H., Higuchi, S., Matsuda, H., Gong, W., Kawasaki, T., Harjo, S., Umezawa, O., 2022. Evolution of dislocation structure determined by neutron diffraction line profile analysis during tensile deformation in quenched and tempered martensitic steels. Mater. Sci. Eng.: A 854, 143795.
Dorin, T., Deschamps, A., Geuser, D., Sigli, C., 2014. Quantification and modelling of the microstructure/strength relationship by tailoring the morphological parameters of the T1 phase in an Al–Cu–Li alloy. Acta Mater. 75, 134–146.
Farid, U., Yan, B., Ruslan, V., 2021. Large and severe plastic deformation of metals: similarities and differences in flow mechanics and structure formation. Adv. Eng. Mater. 23, 2100110.
Heinz, A., Haszler, A., Keidel, C., Moldenhauer, S., Benedictus, R., Miller, W., 2000. Recent development in aluminium alloys for aerospace applications. Mater. Sci. Eng.: A 280, 102–107.
Holt, D., 1970. Dislocation cell formation in metals. J. Appl. Phys. 41, 3197–3201.
Kawka, M., Makinouchi, A., 1996. Plastic anisotropy in FEM analysis using degenerated solid element. J. Mater. Process. Technol. 60, 239–242.
Kida, S., Itoh, T., Sakane, M., Ohnami, M., Socie, D., 1997. Dislocation structure and non-proportional hardening of type 304 stainless steel. Fatigue Fract. Eng. Mater. Struct. 20, 1375–1386.
Li, H., Zhan, L., Huang, M., Zhao, X., Zhou, C., Qiang, Z., 2021. Effects of pre-strain and stress level on stress relaxation ageing behaviour of 2195 Al–Li alloy: experimental and constitutive modelling. J. Alloys. Compd. 851, 156829.
Li, H., Zhang, H., Peng, W., Jiang, Z., Feng, G., Hu, J., Ma, K., Zhan, L., 2023a. Effect of stress level on anisotropy in creep ageing behaviour of 2195-T84 AlLi alloy. Mater. Charact. 206, 113426.
Li, Y., Hou, T., Huang, X., Gao, Y., Zeng, Y., Li, D., 2023b. Constitutive modelling of coupled creep deformation and age hardening behavior of aluminum alloys under various thermal and mechanical loadings. J. Mater. Res. Technol. 25, 333–353.
Li, Y., Shi, Z., Lin, J., Yang, Y., Huang, B., Chung, T., Yang, J., 2016. Experimental investigation of tension and compression creep-ageing behaviour of AA2050 with different initial tempers. Mater. Sci. Eng.: A 657, 299–308.
Li, Y., Shi, Z., Lin, J., Yang, Y., Rong, Q., Huang, B., Chung, T., Tsao, C., Yang, J., Balint, D., 2017. A unified constitutive model for asymmetric tension and compression creep-ageing behaviour of naturally aged Al-Cu-Li alloy. Int. J. Plast. 89, 130–149.
Lian, J., Shen, F., Jia, X., Ahn, D., Chae, D., Münstermann, S., Bleck, W., 2018. An evolving non-associated Hill48 plasticity model accounting for anisotropic hardening and r-value evolution and its application to forming limit prediction. Int. J. Solids. Struct. 151, 20–44.
Liu, C., Yang, J., Ma, P., Ma, Z., Zhan, L., Chen, K., Huang, M., Li, J., Li, Z., 2020. Large creep formability and strength–ductility synergy enabled by engineering dislocations in aluminum alloys. Int. J. Plast. 134, 102774.
Ma, Z., Zhan, L., Liu, C., Xu, L., Xu, Y., Ma, P., Li, J., 2018. Stress-level-dependency and bimodal precipitation behaviors during creep ageing of Al-Cu alloy: experiments and modeling. Int. J. Plast. 110, 183–201.
Peng, N., Zhan, L., Xu, Y., Liu, C., Ma, B., Chen, K., Ren, H., 2022. Anisotropy in creep-aging behavior of Al–Li alloy under different stress levels: experimental and constitutive modeling. J. Mater. Res. Technol. 20, 3456–3470.
Pinheiro, P., Monteiro, W., Barbosa, R., Cetlin, P., 2004. The effect of strain path on the mechanical behavior and dislocation arrangements in the hot working of copper. Mater. Sci. Eng.: A 368, 280–285.
Rodgers, B., Prangnell, P., 2016. Quantification of the influence of increased pre-stretching on microstructure-strength relationships in the Al–Cu–Li alloy AA2195. Acta Mater. 108, 55–67.
Rong, Q., Li, Y., Shi, Z., Meng, L., Sun, X., Lin, J., 2019. Experimental investigations of stress-relaxation ageing behaviour of AA6082. Mater. Sci. Eng.: A 750, 108–116.
Rong, Q., Shi, Z., Li, Y., Lin, J., 2021. Constitutive modelling and its application to stress-relaxation age forming of AA6082 with elastic and plastic loadings. J. Mater. Process. Technol. 295, 117168.
Roters, F., Raabe, D., Gottstein, G., 2000. Work hardening in heterogeneous alloys—A microstructural approach based on three internal state variables. Acta Mater. 48, 4181–4189.
Sakharova, N., Fernandes, J., 2006. Strain path change effect on dislocation microstructure of multicrystalline copper sheets. Mater. Chem. Phys. 98, 44–50.
Thompson, A., 1977. Substructure strengthening mechanisms. Metall. Trans. A 8, 833–842.
Tong, C., Li, Y., Shi, Z., 2020. Investigation of anisotropic creep-ageing behaviour of Al-Cu-Li alloy AA2050. Procedia Manuf. 50, 241–247.
Viatkina, E., Brekelmans, W., Geers, M., 2007. Modelling the evolution of dislocation structures upon stress reversal. Int. J. Solids. Struct. 44, 6030–6054.
Wang, X., Rong, Q., Shi, Z., Li, Y., Cao, J., Chen, B., Lin, J., 2022a. Investigation of stress effect on creep, precipitation and dislocation evolution of Al–Li alloy during creep age forming. Mater. Sci. Eng.: A 836, 142723.
Wang, X., Rong, Q., Shi, Z., Lin, J., 2022b. Improved creep behaviour for a high strength Al-Li alloy in creep age forming: experimental studies and constitutive modelling. Int. J. Plast. 159, 103447.
Wang, X., Rong, Q., Shi, Z., Lin, J., 2023a. An efficient closed-form solution for springback prediction and compensation in elastic–plastic creep age forming. Int. J. Adv. Manufact. Technol. 125, 1115–1133.
Wang, X., Shi, Z., Lin, J., 2023b. Experimental study and modelling of anisotropic behaviour of aluminium-lithium alloys in creep age forming. Int. J. Mech. Sci. 260, 108659.
Wang, X., Shi, Z., Sun, C., Lin, J., 2023c. Investigation of anisotropy evolution of an aluminium-lithium alloy with increasing pre-deformation in creep age forming. Mater. Charact. 206, 113378.
Wejdemann, C., Poulsen, H., Lienert, U., Pantleon, W., 2013. In situ observation of the dislocation structure evolution during a strain path change in copper. JOM 65, 35–43.
Xia, F., Zhan, L., Liao, H., Xu, Y., Chen, K., Ma, B., Liu, C., Zhou, C., Yang, Y., Huang, M., 2023. Effect of different pre-treatments on anisotropy in stress relaxation aging behavior of AA2195 alloy. Mater. Charact. 196, 112610.
Xu, Y., Zhan, L., Huang, M., Liu, C., Wang, X., 2018. Anisotropy in creep-ageing behavior of textured Al-Cu-Mg alloy. Int. J. Lightwe. Mater. Manufact. 1, 40–46.

Yang, H., 2013. Creep Age Forming Investigation On Aluminium Alloy 2219 and Related Studies. Imperial College London. PhD thesis.
Yang, Y., Zhan, L., Liu, C., Wang, X., Wang, Q., Tang, Z., Li, G., Huang, M., Hu, Z., 2020. Stress-relaxation ageing behavior and microstructural evolution under varying initial stresses in an Al–Cu alloy: experiments and modeling. Int. J. Plast. 127, 102646.
Zhan, L., Lin, J., Dean, T., 2011a. A review of the development of creep age forming: experimentation, modelling and applications. Int. J. Mach. Tools Manufact. 51, 1–17.
Zhan, L., Lin, J., Dean, T.A., Huang, M., 2011b. Experimental studies and constitutive modelling of the hardening of aluminium alloy 7055 under creep age forming conditions. Int. J. Mech. Sci. 53, 595–605.
Zhang, L., Li, H., Bian, T., Wu, C., Gao, Y., Lei, C., 2022. Advances and challenges on springback control for creep age forming of aluminum alloy. Chine. J. Aeronaut. 35, 8–34.
Zhao, T., Fan, Z., Xie, H., Chen, H., Chen, S., Zhang, S., 2022. A new modeling framework for anisotropic yield strength of Al-Li alloy sheet with inhomogeneous plate-like T1 precipitates. Int. J. Plast. 157, 103396.
Zheng, J., Lin, J., Lee, J., Pan, R., Li, C., Davies, C., 2018. A novel constitutive model for multi-step stress relaxation ageing of a pre-strained 7xxx series alloy. Int. J. Plast. 106, 31–47.